A Computational Study: The Effect of Hypersonic Plasma Sheaths on Radar Cross Section for Over the Horizon Radars

THESIS

Zachary W. Hoeffner, 1Lt, USAF

AFIT-ENP-MS-17-M097

DEPARTMENT OF THE AIR FORCE
AIR UNIVERSITY

AIR FORCE INSTITUTE OF TECHNOLOGY

Wright-Patterson Air Force Base, Ohio

AFIT-ENP-MS-17-M097

A COMPUTATIONAL STUDY: THE EFFECT OF HYPERSONIC PLASMA SHEATHS ON RADAR CROSS SECTION FOR OVER THE HORIZON RADARS

THESIS

Presented to the Faculty

Department of Engineering Physics

Graduate School of Engineering and Management

Air Force Institute of Technology

Air University

Air Education and Training Command

in Partial Fulfillment of the Requirements for the

Degree of Master of Science in Applied Physics

Zachary W. Hoeffner, B.S.

1Lt, USAF

February 28, 2017

AFIT-ENP-MS-17-M097

A COMPUTATIONAL STUDY: THE EFFECT OF HYPERSONIC PLASMA SHEATHS ON RADAR CROSS SECTION FOR OVER THE HORIZON RADARS

THESIS

Zachary W. Hoeffner, B.S.
1Lt, USAF

Committee Membership:

Maj C. D. Lewis
Chair

Lt Col J. R. Fee
Member

Abstract

The plasma generated around a hypersonic vehicle traveling in the atmosphere has the potenial to alter the vehicle's radar cross section. In this study radar cross sections were calculated for an axial symmetric 6-degree half angle blunted cone with a nose radius of 2.5 cm and length of 3.5 m including and excluding the effects of an atmospheric hypersonic plasma sheath for altitudes of 40 km, 60 km and 80 km and speeds of 5 km/s, 6 km/s and 7 km/s. Free stream atmospheric density and temperature conditions were taken from the 1976 U. S. Standard Atmosphere. A NASA developed code, LAURA, was used to determine the plasma characteristics for the hypersonic flight conditions using a 11-species 2-temperature chemical model. Runs were accomplished first with a super-catalytic surface boundary condition without a turbulence model and then for some cases with an non-reactive surface boundary condition where a mentor-SST turbulence model was used. The resulting plasma sheath properties were used to determine the plasma conductivity around the cone for use in a Finite Difference Time Domain code to calculate the cone's electromagnetic scattering from a plane wave source. A near-field to far-field transformation was used to calculate the radar cross section both with and without the effects of the plasma sheath. The largest increase in radar cross section (RCS) was found for the 60 km 7km/s case with an increase of 3.84%. A possible small decrease in RCS was found for the 40 km altitude 5 km/s and 80 km 7 km/s cases on the order of 0.1%

Acknowledgements

For if any man who never saw fire proved by satisfactory arguments that fire burns. His hearer's mind would never be satisfied, nor would he avoid the fire until he put his hand in it that he might learn by experiment what argument taught.

- Roger Bacon

Thanks to my wife who has given me the support and freedom to enable my hard work.

Thanks to my advisor and comitee members for their advice, guidance, and direction through my computational and theoretical stuggles and developements

Zachary W. Hoeffner

Table of Contents

List of Figures

Figure Page

List of Tables

A COMPUTATIONAL STUDY: THE EFFECT OF HYPERSONIC PLASMA SHEATHS ON RADAR CROSS SECTION FOR OVER THE HORIZON RADARS

I. Introduction

Hypersonic glide vehicles are often classified as aerobodies that travel at speeds in excess of five times the speed of sound using lift within the upper atmosphere to obtain maneuverability beyond that of a traditional ballistic trajectory. The United States, China, and Russia all have had recent flight test programs using these types of vehicles. Examples include the United State's HTV-2, China's DZ-ZF, and Russia's Yu-74, other countries including India, Israel, Japan, and Pakistan are thought to also have active development programs [1].

There are a number operational uses purposed for employing hypersonic vehicles including anti access area denial (A2/AD), A2/AD penetration, and medium to long range precision strike capability for both conventional and nuclear employment [1] [2]. The unique features of these vehicles including high speed maneuvering ability granting non-ballistic trajectories, extended range due to the use of lifting forces, and active target precision make them challenging threat to traditional systems. Although the United States has an established defense architecture for the threat of standard ballistic missiles, a report by the National Academies of Sciences, Engineering, and Medicine, commissioned by the United States Air Force in 2016 suggest against the emerging threat of hypersonic vehicles little to no such architecture exists [2]. A proposed U. S. National Defense Authorization Act for FY2017 specifically rests 25 million dollars of funding on a mandate for the development of a program of record

for hypersonic boost glide vehicle defense which demonstrates significant interest in this issue [3].

Currently, radar is one system that offers the potential to detect the emerging threat of hypersonic boost glide vehicles. Over the Horizon Radar (OTHR) observes reflections from objects beyond the line of sight horizon utilizing skywave and ground wave phenomena. One of the two main types of OTHR is called Skywave radar, it utilizes the electromagnetic reflectivity of the Earth's ionospheric plasma to reflect radar signals over the horizon. This ability to 'see' over the horizon is gives OTHR a significant advantage in surveillance utility compared to traditional line of sight radars which usually assume a direct reflection off of an object. This advantage allows skywave OTHR detection distances up to 1000-4000 km in contrast to a line of sight radar system that even at 1 km in the air could only have a line of sight of 112 km for objects near the ground [4, pg. 1]. For this reason OTHR is often used for long range aircraft detection and surveillance. The very long detection distance allows much earlier detection than other types of radar systems, which is important for hypersonic vehicles which can travel at speeds up to 7 km/s. In order to reflect off of the ionosphere the radar waves must operate with a frequency lower than the plasma frequency of the ionosphere, this limits the typical upper bound on the frequency of OTHR to 3-30 MHz. The ability of a radar system to detect and identify an object is highly dependent on the amount of energy that object reflects back to the radar receiver, the measurement of proportionally how much energy is reflected back to a receiver by an object is known as an object's radar cross section (RCS).

The ability to properly determine the radar cross section of a hypersonic vehicle has valuable detection and tracking applications as experimentation with their use increases around the world. An important aspect of determining the effective radar cross section of a hypersonic vehicle is the effect of the vehicle's plasma sheath that

it creates as it moves in the atmosphere at hypersonic speeds from the ablation of material off of the vehicle's surface and compressive heating of the atmosphere itself. Due to electromagnetic interactions this plasma sheath can refract, reflect, and attenuate the incident radar wave to alter the signal received by the radar station in ways a non sheathed aircraft body would not. Knowledge about the properties of the plasma that surrounds a hypersonic vehicle and the way in which electromagnetic radiation propagation is affected by them will help to evaluate the potential effects of this plasma on the radar cross section of hypersonic vehicles. This study quantifies the effects of the plasma sheath on a hypersonic blunted cone's radar cross section for three speeds 4 km/s, 5 km/s, and 6km/s, each at three altitudes of 40 km, 60 km, and 80 km above sea level for a total of nine test conditions.

The approach taken by this study is to use computational modeling of the physics involved to study this problem. The radial symmetry of the blunted cone is used to simplify the computations to the realm of 2D space. Both the characteristics of the plasma around the hypersonic vehicle and the way in which it interacts with incident radar waves will be obtained by running numerical simulations to solve the differential equations which model the physical system. The basic equations which govern the physical properties of the plasma sheath are the Navier-Stokes equations and the fluid energy equations. The interaction of the incident radar wave with the plasma sheath and the underlying vehicle is governed by Maxwell's Equations. An overview of these equations, the physics behind them, and the way in which they can be treated numerically is given in the theory section of this study. The subsequent chapters will: describe the underlying scientific theory used in the computational codes, discuss the methodology used in this study to preform our computational experiments, analyze the results of our experiments and their implications, and conclude with talk about future work and considerations.

II. Theory

The computational work done in this study uses numerical iteration to approximate the physical behavior behind the phenomena being studied. It is important to identify the underlying equations used in physics that govern this physical behavior and understand their meaning. The three main areas of physics which govern the radar cross section of an object surrounded by a plasma sheath and will be discussed are: the navier-stokes and associated energy equations which determine the properties of the fluid, Maxwell's equations which govern the propagation behavior of the radar wave through the plasma, and the scattering of an electromagnetic wave off of an object which is also governed by Maxwell's equations. In addition to these three areas of physics which are important to understanding the results of the study the techniques and associated effects of numerical iteration itself will also be demonstrated and discussed below.

2.1 Describing a Fluid with the Navier-Stokes Equations

The Navier-Stokes Equations are a system of differential equations used to model the properties of a fluid through the use of conservation of momentum. Along with the equations for conservation of mass, energy, and an equation of state they can be used to solve for the behavior of a fluid subject to boundary conditions. The derivation of these equations starts by deriving the equation for conservation of mass within the fluid. The first step is to imagine an infinitesimal volume of the fluid, dV. The mass within this infinitesimal volume is then given by the integral of the density $\rho(x, y, z, t)$ through out the volume. The change in this total mass over time must be equal to the net amount of mass that enters or leaves the volume which is represented by the integral of the density times fluid velocity $v_i(x, y, z, t)$ at every point on the

surface, dS,

$$\frac{\partial}{\partial t}\int \rho \, dV = -\int \rho v_i \hat{n}_i \, dS \tag{1}$$

where $\hat{n}_i$ is the normal unit vector pointing out of the surface and the Einstein summation convention is used. This convention is a compact way of writing the equation out for each basis vector, in typical Cartesian coordinates, i= x, y, z. . If the same letter subscript is found repeated in a single multiplicative term that implies the term represents a sum over each of the three basis vectors.

Using the divergence theorem, the right hand side of Equation 1 can also be written in the form of a volume integral of the divergence of the density times the fluid velocity. The partial derivative with respect to time is then brought into the integral since it is independent of volume.

$$\int \frac{\partial}{\partial t}\rho \, dV = -\int \frac{\partial}{\partial x_i}(\rho v_i) dV \tag{2}$$

Next, since the infinitesimal volume integral is arbitrary in size it is discarded and both integrands are set equal to each other to obtain our differential equation for conservation of mass within the fluid.

$$\frac{\partial \rho}{\partial t} = -\frac{\partial(\rho v_i)}{\partial x_i} \tag{3}$$

To derive the momentum equations for the fluid the same argument for momentum is used as that for mass except rather than being conserved the source of change for

momentum in the x direction is sum of all forces in the x direction as stated by Newton's second law.

$$\frac{\partial(\rho v_j)}{\partial t} + \frac{\partial(\rho v_j v_i)}{\partial x_i} = \sum F_j \tag{4}$$

The left hand side of this equation can be simplified by applying the chain rule and then applying the relation obtained from conservation of mass to get:

$$v_j \frac{\partial \rho}{\partial t} + \rho \frac{\partial v_j}{\partial t} + \rho v_i \frac{\partial v_j}{\partial x_i} + v_j \frac{\partial(\rho v_i)}{\partial x_i} = \sum F_j \tag{5}$$

$$\rho \frac{\partial v_j}{\partial t} + \rho v_i \frac{\partial v_j}{\partial x_i} = \sum F_j \tag{6}$$

The forces on the right hand side of the equation are further identified by explicitly writing out the internal forces due to the differential changes in normal and shear stress, where σ_{ij} is the stress tensor.

$$\rho \frac{\partial v_j}{\partial t} + \rho v_i \frac{\partial v_j}{\partial x_i} = \frac{\partial}{\partial x_j} \sigma_{ij} + \sum F_j^{body} \tag{7}$$

The Newtonian relations for these normal and shear stress components associated with viscosity are given below where μ is dynamic viscosity, associated with linear deformation, and λ is the second viscosity, associated with volumetric deformation:

$$\sigma_{ij} = \tau_{ij} - p\delta_{ij} \tag{8}$$

$$\tau_{ij} = \mu \left(\frac{\partial v_j}{\partial x_i} + \frac{\partial v_i}{\partial x_j} \right) + \lambda \left(\frac{\partial v_k}{\partial x_k} \right) \delta_{ij} \tag{9}$$

These definitions are then plugged in into Equation 7 and the Stokes hypothesis which suggests a value of $-\frac{2}{3}\mu$ for λ is used to obtain the Navier-Stokes equations for a compressible fluid [5, pg. 398]:

$$\rho\frac{\partial v_j}{\partial t} + \rho v_i\frac{\partial v_j}{\partial x_i} = -\frac{\partial}{\partial x_j}(p + \frac{2\mu}{3}\frac{\partial v_k}{\partial x_k}) + \quad \mu\frac{\partial}{\partial x_j}\left(\frac{\partial v_j}{\partial x_i}\right) + \mu\frac{\partial}{\partial x_j}\left(\frac{\partial v_i}{\partial x_j}\right) + \sum F_j^{body} \tag{10}$$

The physical meaning of Equation 10 is as follows, the first term on the left hand side represents the change in momentum of the fluid at a particular point as time passes, the second term represents the change in a fluid's momentum as it moves to a different location over time. The combination of each effect describes a total change in the momentum over time, sometimes referred to as the substantial derivative. On the right hand side the first term represents a decrease in momentum due to climbing a pressure gradient (increased by a viscosity term) in the fluid, the second term represents a source of momentum due to gradients in the flow velocity, the third term represents a change in momentum influenced by a source of flow velocity, and the final term represents the contribution of body forces on the fluid to its changing momentum.

One useful comparison of terms in this equation is between the so called inertial force of the flow represented by the second term on the left hand side of the equation and the frictional forces represented by the viscous forces of the second and third terms on the right hand side of Equation 10. The inertial force is increased by fluid density and fluid velocity, while the frictional forces are increased by viscosity and an additional length derivative which can be thought of as being inversely proportional to a characteristic length scale L over which we expect to see changes in the fluid. The ratio of these two weighting factors can show how the fluid will behave and is called the Reynolds number, Re,

$$Re = \frac{\rho V}{\frac{\mu}{L}} = \frac{\rho V L}{\mu} \tag{11}$$

At smaller Reynolds numbers small disturbances that perturb the system are smoothed and diffused away due to the larger viscosity of the fluid. At higher Reynolds numbers the inertial forces of these disturbances over power the viscosity and are no longer dissipated leading to turbulence.

To derive the formula for conservation of energy the argument from the conservation of momentum derivation is paralleled, only instead of a change in momentum being due to a force, a change in energy of a system is due to heat and work. The work rate of the fluid can alternatively be written as the net stress flow rate into the system and the time rate of heat increase can like wise be replaced with the net flow of heat into the system.

$$\frac{\partial E}{\partial t} + \frac{\partial (E v_i)}{\partial x_i} = \sum \dot{W} + \sum \dot{Q} \tag{12}$$

$$\frac{\partial E}{\partial t} + \frac{\partial E v_i}{\partial x_i} = \frac{\partial}{\partial x_j}\left(v_i \sigma_{ji}\right) + \frac{\partial q_k}{\partial x_k} \tag{13}$$

$$\frac{\partial E}{\partial t} + \frac{\partial E v_i}{\partial x_i} = -\frac{\partial (p + \frac{2\mu}{3}\frac{\partial v_k}{\partial x_k}) v_j}{\partial x_j} + \mu \frac{\partial}{\partial x_j}\left(v_i \frac{\partial v_j}{\partial x_i}\right) + \mu \frac{\partial}{\partial x_j}\left(v_i \frac{\partial v_i}{\partial x_j}\right) + \frac{\partial q_k}{\partial x_k} \tag{14}$$

The use of these three conservation laws along with an equation of state creates a system of differential equations that can be solved numerically. However at higher Reynolds numbers very small perturbations in the fluid's velocity and pressure are no longer dampened out and must be taken into consideration. The scale of these perturbations can be on the order of micrometers while the scale of objects in the flow is often of meters to tens of meters. The very large range of scale makes it very com-

putationally intensive to run the numerical solvers at the lower scales directly, called direct numerical simulation (DNS). Instead a strategy of using Reynolds-Averaged Navier-Stokes equations is preferentially used. This method takes the fluid properties of velocity and pressure and defines them as an average value plus a random perturbation.

$$v_j = \bar{v_j} + v_j' \tag{15}$$

$$p = \bar{p} + p' \tag{16}$$

These value are then plugged back into the Navier-Stokes equations yielding:

$$\begin{aligned}\frac{\partial \rho(\bar{v_j} + v_j')}{\partial t} + \frac{\partial \rho(\bar{v_i} + v_i')(\bar{v_j} + v_j')}{\partial x_i} = -\frac{\partial}{\partial x_j}(\bar{p} + p' + \frac{2\mu}{3}\frac{\partial(\bar{v_k} + v_k')}{\partial x_k}) + \\ \mu\frac{\partial}{\partial x_j}\left(\frac{\bar{v_j} + v_j'}{\partial x_i}\right) + \mu\frac{\partial}{\partial x_j}\left(\frac{\bar{v_i} + v_i'}{\partial x_j}\right) \\ + \sum F_j^{body}\end{aligned} \tag{17}$$

This new Navier-Stokes equation is averaged over time so that any single perturbation term averages to zero and what is left is a similar equation to the original Navier-Stokes equation except the time dependence has been averaged out and there is now a cross term of the two velocity perturbations:

$$\begin{aligned}\frac{\partial \rho(\bar{v_i}\bar{v_j} + \overline{v_i'v_j'})}{\partial x_i} = -\frac{\partial}{\partial x_j}(\bar{p} + \frac{2\mu}{3}\frac{\partial \bar{v_k}}{\partial x_k}) \\ + \mu\frac{\partial}{\partial x_j}\left(\frac{\partial \bar{v_j}}{\partial x_i}\right) + \mu\frac{\partial}{\partial x_j}\left(\frac{\partial \bar{v_i}}{\partial x_j}\right) + \sum F_j^{body}\end{aligned} \tag{18}$$

Boussinesq proposed that the time average of the product of the velocity fluctu-

ations could be modeled using a viscosity like set of terms [5, pg. 97]. This has the effect of adding an additional viscosity component that increases fluid viscosity by μ_T:

$$-\rho\overline{v_i'v_j'} = 2\mu_T\left(\frac{\partial\bar{v_j}}{\partial x_i} + \frac{\partial\bar{v_i}}{\partial x_j}\right) - \frac{2}{3}\rho k\delta_{ij} \tag{19}$$

Where k is the turbulent kinetic energy defined, μ_T the eddy viscosity, and ω is the specific turbulence dissipation which are given as [6]:

$$k = \frac{1}{2}\overline{v_i'v_i'} \tag{20}$$

$$\mu_T = \frac{\rho k}{\tilde{\omega}} \tag{21}$$

$$\tilde{\omega} = max\left[\omega, C_{lim}\sqrt{\frac{2\left(\frac{\partial\bar{v_j}}{\partial x_i} + \frac{\partial\bar{v_i}}{\partial x_j}\right)\left(\frac{\partial\bar{v_j}}{\partial x_i} + \frac{\partial\bar{v_i}}{\partial x_j}\right)}{\beta^*}}\right] \tag{22}$$

This new term k has its own transport equation along with the specific turbulence dissipation ω in the commonly used $k-\omega$ turbulence model. There are a number of closure parameters in this turbulence model given by: Pr_T, C_{lim}, α, β, β^*, σ, σ^*, σ_d and others, their discussion are outside the scope of this paper and can be found in [6]. The transport equations whose derivations are reproduced in this chapter can be neatly summarized with a more general transport equation often expressed in terms of a general fluid property ϕ as shown in Equation 23:

$$\frac{\partial(\rho\phi)}{\partial t} + \frac{\partial(\rho v_i\phi)}{\partial x_i} = \frac{\partial}{\partial x_i}\left[\Gamma_\phi\frac{\partial\phi}{\partial x_i}\right] + S_\phi \tag{23}$$

where Γ_ϕ acts as a diffusion coefficient and S_ϕ is a source term values of these terms for specific quantities are shown in Table 1.

Table 1. Values of ϕ, Γ_ϕ, and S_ϕ for the transport equation

Property	ϕ	Γ_ϕ	S_ϕ
Mass	1	0	0
Velocity	x_i	$\mu + \mu_T$	$-\frac{\partial p}{\partial x_i} + S'_{x_i}$
Enthalpy	h	$\frac{\mu_T}{Pr_T}$	$\frac{\partial}{\partial x_i}\left[\lambda \frac{\partial T}{\partial x_i}\right] + \frac{\partial p}{\partial t} + \frac{\partial}{\partial x_j}\left[v_i \tau_{ji}\right] + S'_T$
Turbulence	k	$\mu + \sigma^* \mu_T$	$\rho \tau_{ji} \frac{\partial v_j}{\partial x_i} - \beta^* \rho \omega k$
Specific Turbulence Dissipation	ω	$\mu + \sigma \mu_T$	$\frac{\alpha \omega}{k} \tau_{ji} \frac{\partial v_j}{\partial x_i} + \frac{\rho \sigma_d}{\omega} \frac{\partial k}{\partial x_i} \frac{\partial \omega}{\partial x_i} - \beta \rho \omega^2$

These combination of these equations are what is used to describe the flow of a fluid.

2.2 Propagation of Electromagnetic Waves in a Plasma

The equations that govern the interactions of electric and magnetic fields are known as Maxwell's Equations. Using these equations the propagation of the incident radar wave, which is an electromagnetic wave, through the plasma sheath and its reflection off of the hypersonic vehicle can be determined. A numerical method called the finite difference time domain (FDTD) method is used in this study to numerically model the radar wave's propagation. An understanding of how Maxwell's equations govern the effects of the plasma on the propagation of an electromagnetic wave is important for understanding the methodology and results of this study. In this vein the equations will be manipulated into what is known as a dispersion relation which shows the relationship between a wave's frequency ω and its propagation vector k. A wave's propagation vector directly determines how the wave propagates in space and its form can be illuminating for what kinds of things effect the wave's propagation.

Maxwell's equations in derivative form are:

$$\nabla \cdot \boldsymbol{E} = \frac{\rho}{\epsilon_0} \tag{24}$$

$$\nabla \times \boldsymbol{E} = -\frac{\partial \boldsymbol{B}}{\partial t} \tag{25}$$

$$\nabla \cdot \boldsymbol{B} = 0 \tag{26}$$

$$\nabla \times \boldsymbol{B} = \mu_0 \boldsymbol{J} + \mu_0 \epsilon_0 \frac{\partial \boldsymbol{E}}{\partial t} \tag{27}$$

Here, $\boldsymbol{E}$ is the electric field, ρ is the free charge, ϵ_0 is the permitivity of free space, $\boldsymbol{B}$ is the magnetic field, μ_0 is the permeability of free space and $\boldsymbol{J}$ is the current density. The electric field can be expanded as an infinite sum of plane waves propagating in the $\boldsymbol{k}$ direction with angular frequency ω and a magnitude of $\tilde{\boldsymbol{E}}(\boldsymbol{k}, \omega)$ defined as :

$$\boldsymbol{E}(\boldsymbol{r}, t) = \frac{1}{(2\pi)^2} \int_{-\infty}^{\infty} \tilde{\boldsymbol{E}}(\boldsymbol{k}, \omega) e^{i(\boldsymbol{k} \cdot \boldsymbol{r} - \omega t)} d^3k d\omega \tag{28}$$

Note in general substituting a function $f(r, t)$ with its corresponding $\tilde{f}(k, \omega)$ is done through a Fourier transform. Under such a transform derivatives with respect to spacial components of $\boldsymbol{r}$ are equivalent to multiplication of the Fourier transform by $i\boldsymbol{k}$ and derivatives with respect to t are equivalent to multiplication by $-i\omega$. Maxwell's Equations under Fourier transform become:

$$i\boldsymbol{k} \cdot \tilde{\boldsymbol{E}} = \frac{\tilde{\rho}}{\epsilon_0} \tag{29}$$

$$i\boldsymbol{k} \times \tilde{\boldsymbol{E}} = i\omega \tilde{\boldsymbol{B}} \tag{30}$$

$$i\boldsymbol{k} \cdot \tilde{\boldsymbol{B}} = 0 \tag{31}$$

$$i\boldsymbol{k} \times \tilde{\boldsymbol{B}} = \mu_0 \tilde{\boldsymbol{J}} - \mu_0 \epsilon_0 i\omega \tilde{\boldsymbol{E}} \tag{32}$$

here the tilde above the vector designates it is in frequency space.

Next, the current density can be defined as the net sum of the movement of charge density for each species s as:

$$\boldsymbol{J} = \sum_s n_s e_s \boldsymbol{v}_s \tag{33}$$

The velocity of each species can be found using Newton's Second Law $F = m\boldsymbol{a}$

$$m_s \frac{\partial \boldsymbol{v}_s}{\partial t} = e_s(\boldsymbol{E} + \boldsymbol{v}_s \times \boldsymbol{B}) + \sum_t (\boldsymbol{v}_t - \boldsymbol{v}_s) m_s \nu_{st} \tag{34}$$

The first term represents the Coulomb force on the particle and the second term is the drag force on the particle of species s due to collisions with other species t. If the external magnetic field is assumed to be negligible and a Fourier transform is taken Equation 34 becomes:

$$-m_s i\omega \tilde{\boldsymbol{v}}_s = e_s \tilde{\boldsymbol{E}} + m_s \sum_t (\tilde{\boldsymbol{v}}_t - \tilde{\boldsymbol{v}}_s) \nu_{st} \tag{35}$$

If the reference frame is chosen so that the average velocity of the electrons before being perturbed by an incident field is zero, then it is a fairly good assumption that the average velocity of the collisional species t can also be assumed to be zero (or at the very least negligible compared to the velocity of the electrons due to the incident electric field), the solution for $\tilde{\boldsymbol{v}}_s$ after this assumption is:

$$\tilde{\boldsymbol{v}}_s = \frac{-e_s \tilde{\boldsymbol{E}}}{m_s(i\omega - \sum_t \nu_{st})} \tag{36}$$

This term is then substituted into the Fourier transformed current equation to obtain:

$$\tilde{\boldsymbol{J}} = \sum_s \frac{-n_s e_s^2 \tilde{\boldsymbol{E}}}{m_s(i\omega - \sum_t \nu_{st})} \tag{37}$$

This equation for current density is substituted back into Ampere's Law, Equation 32 to get:

$$i\boldsymbol{k} \times \tilde{\boldsymbol{B}} = \mu_0 \sum_s \frac{-n_s e_s^2 \tilde{\boldsymbol{E}}}{m_s(i\omega - \sum_t \nu_{st})} - \mu_0 \epsilon_0 i\omega \tilde{\boldsymbol{E}} \tag{38}$$

A substitution is then made using the definition of the plasma frequency, $\omega_{ps}^2 = \frac{n_s e_s^2}{m_s \epsilon_0}$, to obtain:

$$i\boldsymbol{k} \times \tilde{\boldsymbol{B}} = \mu_0 \epsilon_0 \sum_s \frac{-{\omega_{ps}}^2 \tilde{\boldsymbol{E}}}{i\omega - \sum_t \nu_{st}} - \mu_0 \epsilon_0 i\omega \tilde{\boldsymbol{E}} \tag{39}$$

In order to eliminate the B field from Equation 39, $i\boldsymbol{k}$ is crossed with Equation 30 which allows the left hand side of Equation 39 to be expressed in terms of an electric field. After substitution of the modified Equation 30 and some manipulation this gives:

$$-c^2\boldsymbol{k}\times\boldsymbol{k}\times\tilde{\boldsymbol{E}}=\omega^2\tilde{\boldsymbol{E}}-\sum_s\frac{\omega{\omega_{ps}}^2\tilde{\boldsymbol{E}}}{\omega+i\sum_t\nu_{st}} \tag{40}$$

For a chosen coordinate system that aligns the k vector with the z axis the equation can be rewritten in matrix form as:

$$\begin{bmatrix} -c^2k^2+\omega^2-\sum_s\frac{\omega{\omega_{ps}}^2}{\omega+i\sum_t\nu_{st}} & 0 & 0 \\ 0 & -c^2k^2+\omega^2-\sum_s\frac{\omega{\omega_{ps}}^2}{\omega+i\sum_t\nu_{st}} & 0 \\ 0 & 0 & \omega^2-\sum_s\frac{\omega{\omega_{ps}}^2}{\omega+i\sum_t\nu_{st}} \end{bmatrix}\begin{bmatrix}\tilde{E}_x\\ \tilde{E}_y\\ \tilde{E}_z\end{bmatrix}=\begin{bmatrix}0\\0\\0\end{bmatrix} \tag{41}$$

The dispersion relation is determined by the solutions to this equation, namely for the transverse electric field components:

$$\omega^2=\sum_s\frac{\omega{\omega_{ps}}^2}{\omega+i\sum_t\nu_{st}}+c^2k^2 \tag{42}$$

Solving for k we find:

$$k=\frac{1}{c}\sqrt{\omega^2-\sum_s\frac{\omega{\omega_{ps}}^2}{\omega+i\sum_t\nu_{st}}} \tag{43}$$

which gives an index of refraction:

$$n = \sqrt{1 - \sum_s \frac{{\omega_{ps}}^2}{\omega(\omega + i\sum_t \nu_{st})}} \tag{44}$$

$$= \sqrt{1 - \sum_s [\frac{{\omega_{ps}}^2}{\omega^2 + (\sum_t \nu_{st})^2} - \frac{i\omega_{ps}^2 \sum_t \nu_{st}}{\omega^3 + \omega(\sum_t \nu_{st})^2}]} \tag{45}$$

These resulting equations for k and n are complex and fairly difficult to interpret at first glance. In order to get a better grasp of what they mean a plot of the real and imaginary components of n are shown in Figures 1 and 2 respectively. Table 2 shows the limiting cases obtained by the first order Taylor or Puiseux series for when the value is very small or very large respectively. Interestingly and relevant to the study, the presence of a collision frequency reduces the imaginary component of n and the associated attenuation when the plasma frequency is above the propagation frequency. This is shown in Figure 2 by a decreasing curve with increasing collision frequency when the plasma frequency is larger than 1MHz, the propagation frequency. Contrastingly when the plasma frequency is just less than 1MHz, or just below the propagation frequency, a small collision frequency on the order of 1MHz actually increases the imaginary component of n, indicating that the collision frequency increases attenuation in that case. While increase attenuation happens at lower collisional frequencies, the index of refraction also increases which increases the likely hood the wave will refract or reflect away from that location. In order to determine a balance between these two contradictory considerations a plot of the imaginary component of n divided by the deviation of the real component from 1, the index of refraction for freespace is shown in Figure 3. When both collision frequency and plasma frequency are well above the propagation frequency increasing the collision frequency yields a chance for slightly more attenuation while increasing plasma frequency leads to slightly less.

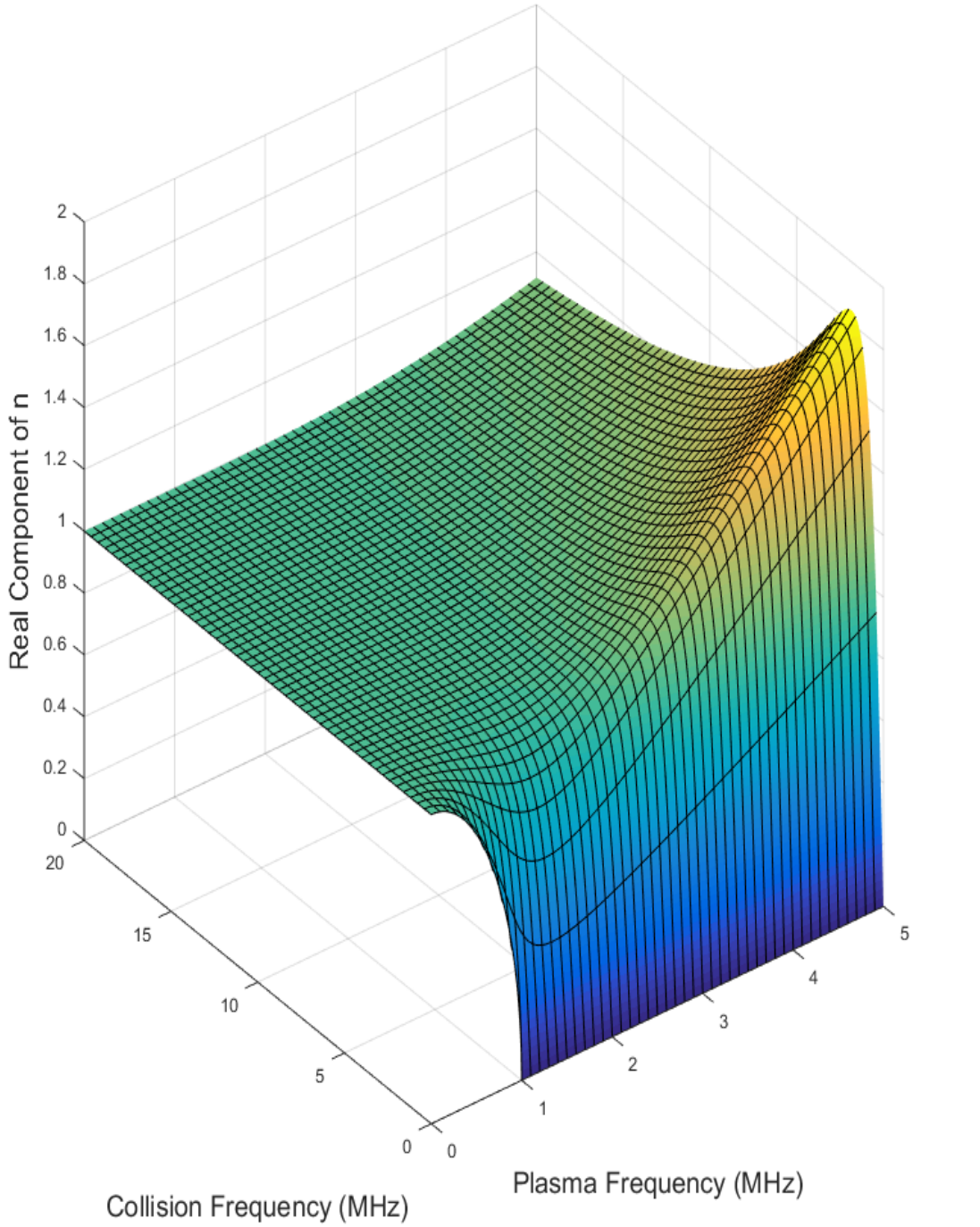

Figure 1. Example of Re(n) for example plasma and collision frequencies

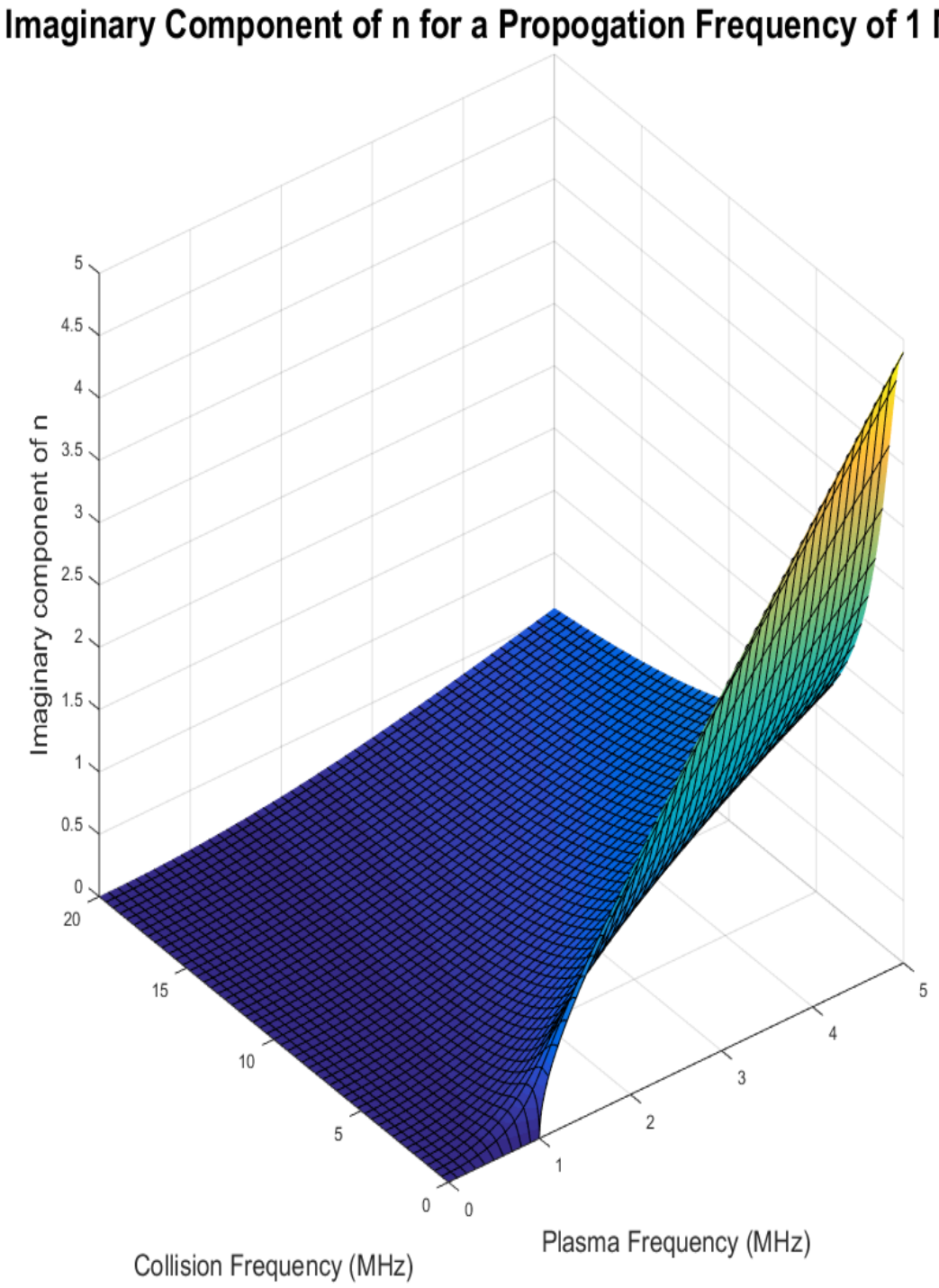

Figure 2. Example of Im(n) for example plasma and collision frequencies

Table 2. Limiting Cases for Real and Imaginary Components for the Index of Refraction
This table containes the limiting cases for real and imaginary solutions to n from Equation 45, they were obtained by taking the first order term from the equation's Taylor or Puiseux expansion for the limitting case of the value being very small or large respectively.

$\frac{\omega_p}{\omega}$	$\frac{\omega_p}{\nu}$	$\frac{\nu}{\omega}$	$Re(n)$	$Im(n)$
> 1	$>> 1$	$>> 1$	$\sqrt{\frac{\omega_p^2\nu}{2\omega\nu^2}}$	$\sqrt{\frac{\omega_p^2\nu}{2\omega\nu^2}}$
< 1	$>> 1$	$>> 1$	$\sqrt{\frac{\omega_p^2\nu}{2\omega\nu^2}}$	$\sqrt{\frac{\omega_p^2\nu}{2\omega\nu^2}}$
> 1	$<< 1$	$>> 1$	1	$\frac{\omega_p^2\nu}{2\omega\nu^2}$
< 1	$<< 1$	$>> 1$	1	$\frac{\omega_p^2\nu}{2\omega\nu^2}$
$<< 1$	$<< 1$	1	$1 - \frac{\omega_p^2}{4\omega^2}$	$\frac{\omega_p^2}{4\omega^2}$
1	1	1	0.777	0.322
$>> 1$	$>> 1$	1	$0.322 * \frac{\omega_p}{\omega}$	$0.777 * \frac{\omega_p}{\omega}$
> 1	$>> 1$	$<< 1$	0	$\sqrt{\frac{\omega_p^2}{\omega^2} - 1}$
< 1	$>> 1$	$<< 1$	$\sqrt{1 - \frac{\omega_p^2}{\omega^2}}$	0
> 1	$<< 1$	$<< 1$	0	$\sqrt{\frac{\omega_p^2}{\omega^2} - 1}$
< 1	$<< 1$	$<< 1$	$\sqrt{1 - \frac{\omega_p^2}{\omega^2}}$	0

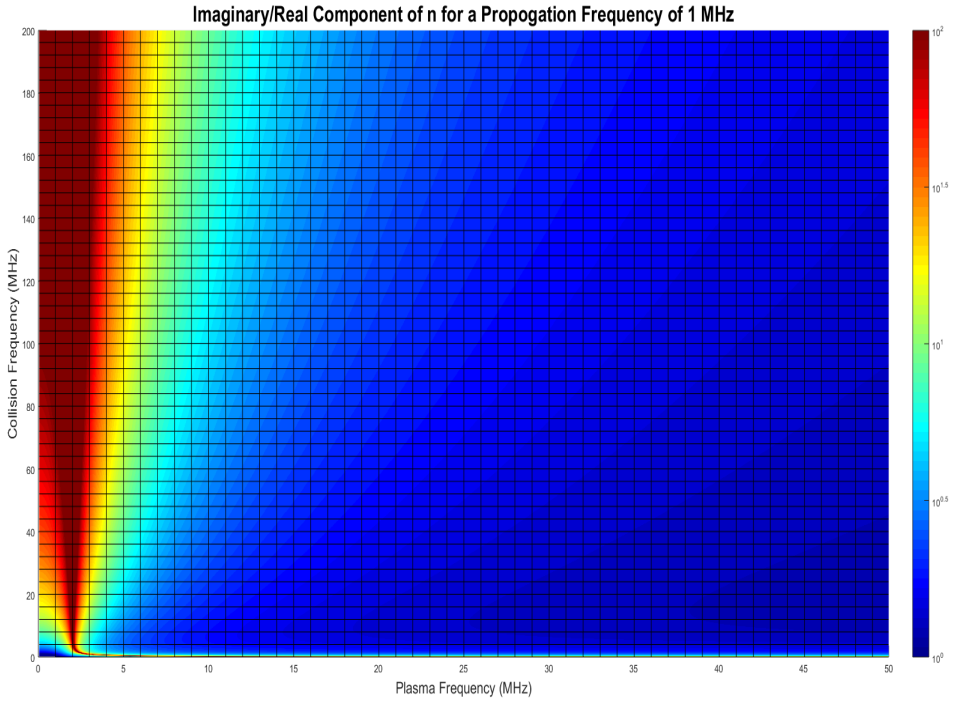

Figure 3. Im(n)/abs(n-1) for example plasma and collision frequencies

2.3 Electromagnetic Scattering and Radar Cross Sections

Electromagnetic Scattering is the study of the ways in which electromagnetic waves are scattered or redirected after being incident upon an object or system. The nature of the interaction between the incident wave and the object is generally governed by the relationship between the object's size relative to the wavelength of the incident wave. For this reason scattering effects are usually defined as having three fairly distinct regions based upon this relationship, the Rayleigh region where the wavelength is much larger than the object's dimensions, the Mie region where the object is has the same order of size as the incident wavelength, and the optical region where the wavelength is much smaller in size than the objects features. Over the horizon radar operates at 3-30 MHz, corresponding to a wavelength of 10 m to 100 m which is larger than the size of the blunted cone indicating that the simulation will operate most closely to the Rayleigh scattering region. In the Rayleigh region since the object is smaller than the wavelength the electromagnetically field can often be treated as inducing electric and magnetic currents which oscillate with the incoming radiation and re-radiate a scattered field [7, pg. 97]. In the case of a computational simulation these currents are found numerically form Maxwell's equations. The differential radar cross section for a 2D scattering object is defined as the ratio of the the incident power of the electromagnetic wave divided by the scattered power. Since the power of the incident and scattered fields are proportional to the square of the electric field it can also be written in terms of the electric field as seen in Equation 46:

$$\frac{d\sigma}{d\phi} = \frac{|\boldsymbol{E}(\phi)_{scattered}|^2}{|\boldsymbol{E}_{incident}|^2} \tag{46}$$

where σ is the total radar cross section, obtained by an integral over all angular

directions ϕ.

2.4 Finite Difference Time Domain (FDTD) Propagation of Electromagnetic Waves in a Plasma

The method used in this study in order to model the propagation of electromagnetic waves in a medium is to discretize Maxwell's differential equations in time and space and then iterate forward in time as the wave propagates. The time and space derivatives are discretized through the use of a Taylor series expansion. The general form of a Taylor series expansion for a function $f(x)$ is:

$$f(x+\Delta x) = \frac{f(x)}{0!} + \frac{\Delta x}{1!}\frac{df(x)}{dx} + \frac{(\Delta x)^2}{2!}\frac{d^2f(x)}{dx^2} + \frac{(\Delta x)^3}{3!}\frac{d^3f(x)}{dx^3} + ... \tag{47}$$

The variable x can then be discretized onto a grid of uniform spacing Δx where x_i represents x at grid point i, x_{i-1} the previous grid point, and x_{i+1} the subsequent one. The Taylor series equation now becomes:

$$f(x_{i+1}) = \frac{f(x_i)}{0!} + \frac{\Delta x}{1!}\frac{df(x_i)}{dx} + \frac{(\Delta x)^2}{2!}\frac{d^2f(x_i)}{dx^2} + \frac{(\Delta x)^3}{3!}\frac{d^3f(x_i)}{dx^3} + ... \tag{48}$$

If Δx is assumed to be small so that 2nd order and higher terms can be ignored, $\frac{df(x_i)}{dx}$ is solved for to find:

$$\frac{df(x_i)}{dx} = \frac{f(x_{i+1}) - f(x_i)}{\Delta x} \tag{49}$$

since this result only takes into account terms of the first order of Δx it is called a

first order approximation.

The procedure can then be repeated using a Taylor series of the function at the points $f(x_{i+1})$ and $f(x_{i-1})$ so that the following system of equations is obtained:

$$f(x_{i+1}) = \frac{f(x_i)}{0!} + \frac{\Delta x}{1!}\frac{df(x_i)}{dx} + \frac{(\Delta x)^2}{2!}\frac{d^2f(x_i)}{dx^2} + \frac{(\Delta x)^3}{3!}\frac{d^3f(x_i)}{dx^3} + ... \tag{50}$$

$$f(x_{i-1}) = \frac{f(x_i)}{0!} + \frac{-\Delta x}{1!}\frac{df(x_i)}{dx} + \frac{(-\Delta x)^2}{2!}\frac{d^2f(x_i)}{dx^2} + \frac{(-\Delta x)^3}{3!}\frac{d^3f(x_i)}{dx^3} + ... \tag{51}$$

Equation 50 is subtracted from 51 to get:

$$f(x_{i+1}) - f(x_{i-1}) = 2\frac{\Delta x}{1!}\frac{df(x_i)}{dx} + 2\frac{(\Delta x)^3}{3!}\frac{d^3f(x_i)}{dx^3} + ... \tag{52}$$

The term $\frac{df(x_i)}{dx}$ is now able to be solved for but notice that the lowest term that must be ignored is now a 3rd power of Δx which means that this is a 2nd order approximation, specifically the 2nd order central difference approximation.

$$\frac{df(x_i)}{dx} = \frac{f(x_{i+1}) - f(x_{i-1})}{2\Delta x} \tag{53}$$

In general if n points are used our system of equations can be represented as a solvable $n \times n$ matrix equation if approximated to the $n-1$ order

$$\begin{bmatrix} f(x_{i+a}) \\ f(x_{i+b}) \\ f(x_{i+c}) \\ f(x_{i+d}) \\ \\ \dots \end{bmatrix} = \begin{bmatrix} 1 & a\Delta x & \frac{(a\Delta x)^2}{2!} & \frac{(a\Delta x)^3}{3!} & \dots \\ 1 & b\Delta x & \frac{(b\Delta x)^2}{2!} & \frac{(b\Delta x)^3}{3!} & \dots \\ 1 & c\Delta x & \frac{(c\Delta x)^2}{2!} & \frac{(c\Delta x)^3}{3!} & \dots \\ 1 & d\Delta x & \frac{(d\Delta x)^2}{2!} & \frac{(d\Delta x)^3}{3!} & \dots \\ \dots & \dots & \dots & \dots & \dots \end{bmatrix} \begin{bmatrix} f(x_i) \\ \frac{df(x_i)}{dx} \\ \frac{d^2f(x_i)}{dx^2} \\ \frac{d^3f(x_i)}{dx^3} \\ \dots \end{bmatrix} \tag{54}$$

Which has the solution:

$$\begin{bmatrix} f(x_i) \\ \frac{df(x_i)}{dx} \\ \frac{d^2f(x_i)}{dx^2} \\ \frac{d^3f(x_i)}{dx^3} \\ \dots \end{bmatrix} = \begin{bmatrix} 1 & a\Delta x & \frac{(a\Delta x)^2}{2!} & \frac{(a\Delta x)^3}{3!} & \dots \\ 1 & b\Delta x & \frac{(b\Delta x)^2}{2!} & \frac{(b\Delta x)^3}{3!} & \dots \\ 1 & c\Delta x & \frac{(c\Delta x)^2}{2!} & \frac{(c\Delta x)^3}{3!} & \dots \\ 1 & d\Delta x & \frac{(d\Delta x)^2}{2!} & \frac{(d\Delta x)^3}{3!} & \dots \\ \dots & \dots & \dots & \dots & \dots \end{bmatrix}^{-1} \begin{bmatrix} f(x_{i+a}) \\ f(x_{i+b}) \\ f(x_{i+c}) \\ f(x_{i+d}) \\ \dots \end{bmatrix} \tag{55}$$

These finite difference approximations for the derivative will be used to discritize Maxwell's equations. In order to numerically propagate an electromagnetic wave in the time domain Yee developed a method in which the discretized electric and magnetic field components are calculated alternatively at half time steps on spacial grids half offset from each other. This gridding technique is known as a Yee cube in 3D and a simplified 2D form is used to take advantage of the radial symmetry present in the conical aerobody.

In Figures 4 and 5, i represents the x gridding coordinate while k represents the z gridding coordinate. Notice that the various components of the E and H fields are not all calculated at the same position only where they are needed for the surrounding component's curl from Maxwell's equations.

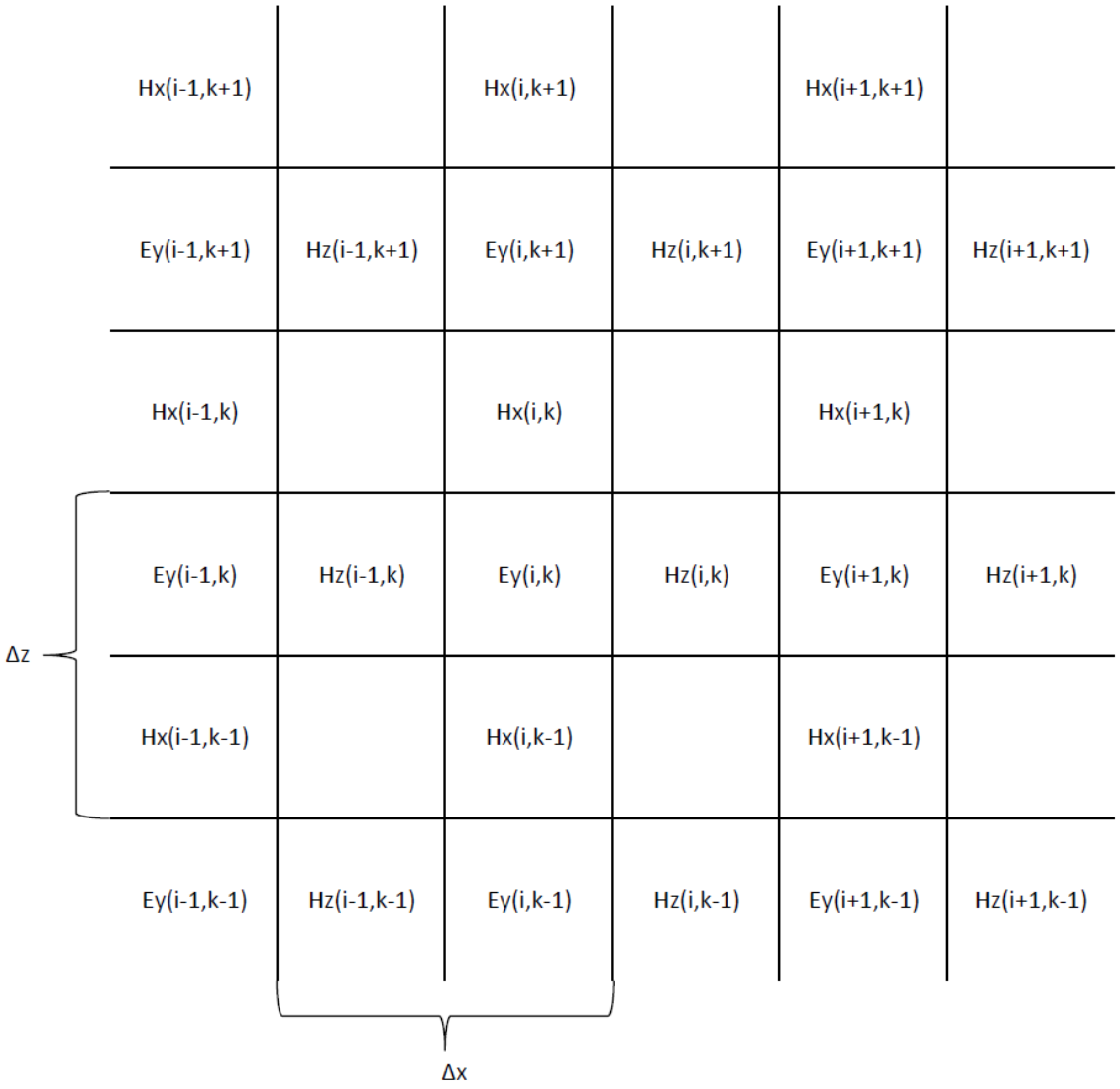

Figure 4. Example of the mesh used for TM wave Yee FDTD propagation simulations

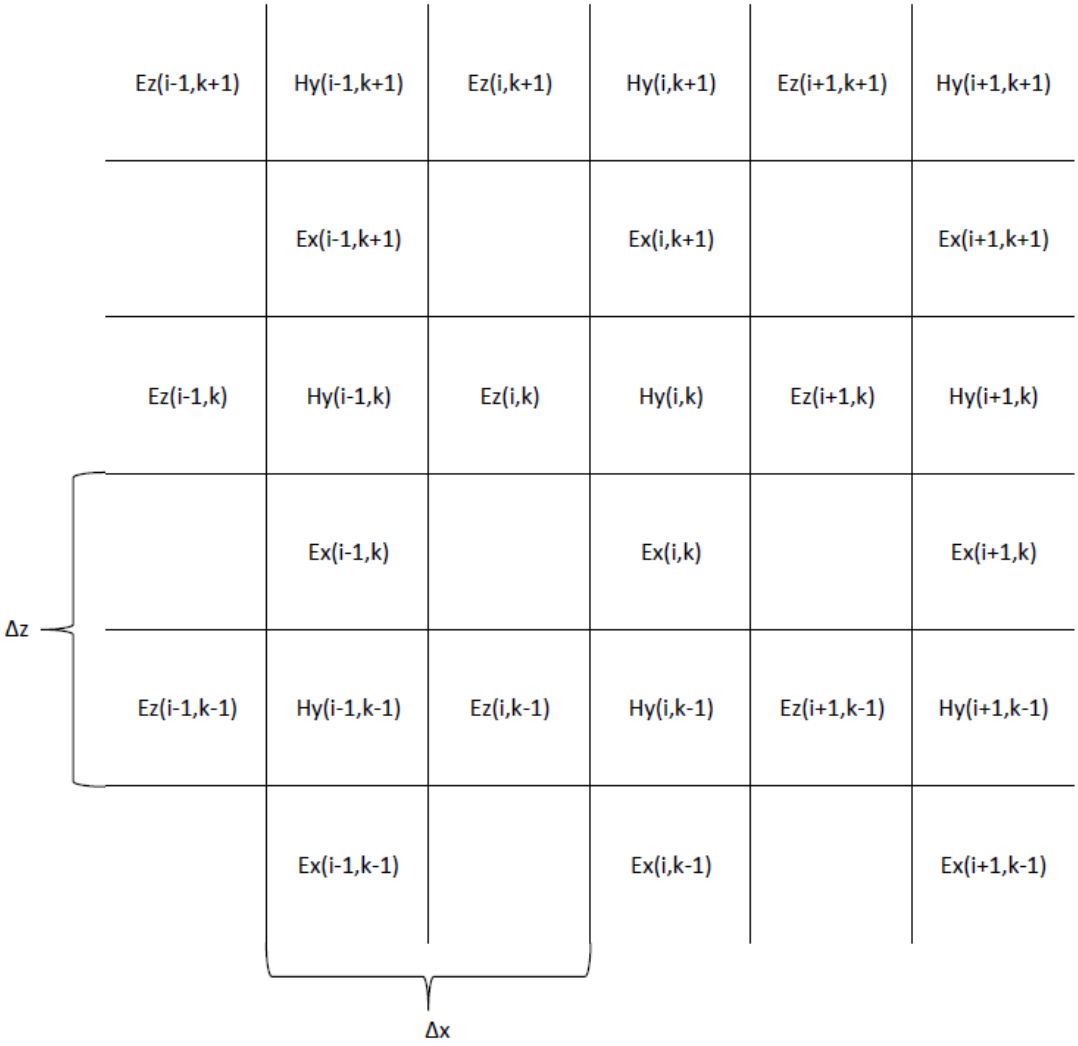

Figure 5. Example of the mesh used for TE wave Yee FDTD propagation simulations

To implement Yee's algorithm, time derivatives of the H and E field components are solved for from the Maxwell curl equations. The axially symmetric nature of the cone and its plasma sheath means that the properties are the same for any planar slice that includes the axis, allowing for a simplification to 2D in one of those planes. The FDTD simulation will be in the 2D x-z plane so that all derivatives with respect to the y direction are zero and not shown. Fictitious terms for magnetic conduction and impressed current are often included which are useful for specifying source terms and effects for the simulated fields which yields [8, pg. 3]:

$$\frac{\partial E_x}{\partial t} = \frac{1}{\epsilon_x}\left(-\frac{\partial H_y}{\partial z} - \sigma_x^e E_x - J_{ix}\right) \tag{56}$$

$$\frac{\partial E_y}{\partial t} = \frac{1}{\epsilon_y}\left(\frac{\partial H_x}{\partial z} - \frac{\partial H_z}{\partial x} - \sigma_y^e E_y - J_{iy}\right) \tag{57}$$

$$\frac{\partial E_z}{\partial t} = \frac{1}{\epsilon_z}\left(\frac{\partial H_y}{\partial x} - \sigma_z^e E_z - J_{iz}\right) \tag{58}$$

$$\frac{\partial H_x}{\partial t} = \frac{1}{\mu_x}\left(\frac{\partial E_y}{\partial z} - \sigma_x^m H_x - M_{ix}\right) \tag{59}$$

$$\frac{\partial H_y}{\partial t} = \frac{1}{\mu_y}\left(-\frac{\partial E_x}{\partial z} + \frac{\partial E_z}{\partial x} - \sigma_y^m H_y - M_{iy}\right) \tag{60}$$

$$\frac{\partial H_z}{\partial t} = \frac{1}{\mu_z}\left(-\frac{\partial E_y}{\partial x} - \sigma_z^m H_z - M_{iz}\right) \tag{61}$$

Next, the finite difference method shown previously in Equation 55 is used to replace the partial derivatives in both time and space with their numerical counterparts for the derivatives. This becomes for E_y and H_y:

$$\frac{\partial E_y}{\partial t} = \frac{1}{\Delta t} \sum_{l=0}^{h} C_l \cdot E_y^{n+1-l}(i,k) \tag{62}$$

$$\frac{\partial H_x}{\partial z} = \frac{1}{\Delta z} \sum_{l=0}^{h} C_l \cdot H_x^{n+1/2}(i,k-h/2+l) \tag{63}$$

$$\frac{\partial H_z}{\partial x} = \frac{1}{\Delta x} \sum_{l=0}^{h} C_l \cdot H_z^{n+1/2}(i-h/2+l,k) \tag{64}$$

$$\frac{\partial H_y}{\partial t} = \frac{1}{\Delta t} \sum_{l=0}^{h} C_l \cdot H_y^{n+1/2-l}(i,k) \tag{65}$$

$$\frac{\partial E_x}{\partial z} = \frac{1}{\Delta z} \sum_{l=0}^{h} C_l \cdot E_x^{n+1/2}(i,k-h/2+l+1) \tag{66}$$

$$\frac{\partial E_z}{\partial x} = \frac{1}{\Delta x} \sum_{l=0}^{h} C_l \cdot E_z^{n+1/2}(i-h/2+l+1,k) \tag{67}$$

Here h is the order of the derivative approximation, l increments in integer steps, and n represents the current time step. The H field is calculated at the half integer time steps and then the E field is calculated at whole integer steps. The grid vectors i and k represent the list of indices in the x and z directions respectively. The variable C_l represents the finite difference coefficient derived in Equation 55 and iterates up through the weighting factors for the corresponding positions. Note that since a central difference method is used to differentiate in space, only even values for h result in integer indices.

These finite difference approximations are substituted in place of the partial derivatives in Maxwell's Equations and examples of this for E_y is shown in Equation 68. After obtaining these new discrete equations the future time steps of the E and H fields can be expressed in terms of the previous time step values. An example

of this process is shown for the future time step for E_y in Equation 69 where the finite difference approximations for H have been written more compactly as ΔH over the respective coordinate.

$$\frac{C_0}{\Delta t} \cdot E_y^{n+1}(i,k) + \frac{1}{\Delta t} \sum_{l=1}^{h} C_l \cdot E_y^{n+1-l}(i,k) = \frac{1}{\epsilon_y(i,k)} \left(\frac{\Delta H_x^{n+1/2}(i,k)}{\Delta z} - \frac{\Delta H_z^{n+1/2}(i,k)}{\Delta x} \right) - \frac{1}{\epsilon_y(i,k)} \left(\sigma_y^e(i,k) E_y^{n+1/2}(i,k) + J_{iy}^{n+1/2}(i,k) \right) \tag{68}$$

$$\begin{aligned} E_y^{n+1}(i,k) = & \frac{\Delta t}{C_0 \epsilon_y(i,k)} \left(\frac{\Delta H_x^{n+1/2}(i,k)}{\Delta z} - \frac{\Delta H_z^{n+1/2}(i,k)}{\Delta x} \right) \\ & - \frac{\Delta t}{C_0 \epsilon_y(i,k)} \left(\sigma_y^e(i,k) E_y^{n+1/2}(i,k) + J_{iy}^{n+1/2}(i,k) \right) \\ & - \sum_{l=1}^{h} \frac{C_l}{C_0} \cdot E_y^{n+1-l}(i,k) \end{aligned} \tag{69}$$

In the Yee algorithm $E_y^{n+1/2}$ is not known since it is at a half integer time step and the Yee formulation only solves for integer time steps of E so it is instead approximated it as the average of the previous and next time step values:

$$E_y^{n+1/2}(i,k) = \frac{E_y^n(i,k) + E_y^{n+1}(i,k)}{2} \tag{70}$$

This approximation is then substituted back into Equation 69 to give:

$$E_y^{n+1}(i,k) = \frac{\Delta t}{C_0 \epsilon_y(i,k)} \left(\frac{\Delta H_x^{n+1/2}(i,k)}{\Delta z} - \frac{\Delta H_z^{n+1/2}(i,k)}{\Delta x} \right) \tag{71}$$

$$- \frac{\Delta t}{C_0 \epsilon_y(i,k)} \sigma_y^e(i,k) \left(\frac{E_y^n(i,k) + E_y^{n+1}(i,k)}{2} \right) \tag{72}$$

$$- \frac{\Delta t}{C_0 \epsilon_y(i,k)} J_{iy}^{n+1/2}(i,k) \tag{73}$$

$$- \sum_{l=1}^{h} \frac{C_l}{C_0} \cdot E_y^{n+1-l}(i,k) \tag{74}$$

An additional E_y^{n+1} term has now been introduced to the right hand side by the approximation for $E_y^{n+1/2}$ and Equation 74 is no longer explicitly solved for E_y^{n+1}. The steps to resolve for E_y^{n+1} are shown in equations 75 through 76:

$$\begin{aligned} E_y^{n+1}(i,k) + \frac{\Delta t \sigma_y^e(i,k)}{2C_0 \epsilon_y(i,k)} \cdot E_y^{n+1}(i,k) = & \frac{\Delta t}{C_0 \epsilon_y(i,k)} \left(\frac{\Delta H_x^{n+1/2}(i,k)}{\Delta z} - \frac{\Delta H_z^{n+1/2}(i,k)}{\Delta x} \right) \\ & - \frac{\Delta t}{C_0 \epsilon_y(i,k)} \sigma_y^e(i,k) \frac{E_y^n(i,k)}{2} \\ & - \frac{\Delta t}{C_0 \epsilon_y(i,k)} J_{iy}^{n+1/2}(i,k) \\ & - \sum_{l=1}^{h} \frac{C_l}{C_0} \cdot E_y^{n+1-l}(i,k) \end{aligned} \tag{75}$$

Combine the like summations in the third term on the right hand side and multiply by $2C_0\epsilon$

$$
\begin{aligned}
(2C_0\epsilon_y(i,k) + \Delta t\sigma_y^e(i,k))E_y^{n+1}(i,k) = 2\Delta t &\left(\frac{\Delta H_x^{n+1/2}(i,k)}{\Delta z} - \frac{\Delta H_z^{n+1/2}(i,k)}{\Delta x}\right) \\
&- 2\Delta t\sigma_y^e(i,k)\frac{E_y^n(i,k)}{2} \\
&- 2\Delta t J_{iy}^{n+1/2}(i,k) \\
&- 2\epsilon_y(i,k)\sum_{l=1}^{h} C_l \cdot E_y^{n+1-l}(i,k)
\end{aligned}
\tag{76}
$$

The final time stepping equation for calculating E_y^{n+1} is shown in Equation 77 which depends only on values of the fields and currents in previous time steps:

$$
\begin{aligned}
E_y^{n+1}(i,k) = &\frac{2\Delta t}{(2C_0\epsilon_y(i,k) + \Delta t\sigma_y^e(i,k))}\left(\frac{\Delta H_x^{n+1/2}(i,k)}{\Delta z} - \frac{\Delta H_z^{n+1/2}(i,k)}{\Delta x}\right) \\
&- \frac{2\Delta t}{(2C_0\epsilon_y(i,k) + \Delta t\sigma_y^e(i,k))}\sigma_y^e(i,k)\frac{E_y^n(i,k)}{2} \\
&- \frac{2\Delta t}{(2C_0\epsilon_y(i,k) + \Delta t\sigma_y^e(i,k))}J_{iy}^{n+1/2}(i,k) \\
&- \frac{2\epsilon_y(i,k)}{(2C_0\epsilon_y(i,k) + \Delta t\sigma_y^e(i,k))}\sum_{l=1}^{h} C_l \cdot E_y^{n+1-l}(i,k)
\end{aligned}
\tag{77}
$$

The same methodology is used to arrive at similar solutions for the other field components shown in equations 78 through 82:

$$
\begin{aligned}
H_y^{n+1/2}(i,k) = & \frac{2\Delta t}{(2C_0\mu_y(i,k)+\Delta t\sigma_y^m(i,k))}\left(\frac{-\Delta E_x^n(i,k)}{\Delta z}+\frac{\Delta E_z^n(i,k)}{\Delta x}\right) \\
& - \frac{2\Delta t}{(2C_0\mu_y(i,k)+\Delta t\sigma_y^m(i,k))}\sigma_y^m(i,k)\frac{H_y^{n-1/2}(i,k)}{2} \\
& - \frac{2\Delta t}{(2C_0\mu_y(i,k)+\Delta t\sigma_y^m(i,k))}M_{iy}^n(i,k) \\
& - \frac{2\mu_y(i,k)}{(2C_0\mu_y(i,k)+\Delta t\sigma_y^m(i,k))}\sum_{l=1}^{h} C_l\cdot H_y^{n+1/2-l}(i,k)
\end{aligned}
\tag{78}
$$

and the others:

$$
\begin{aligned}
E_x^{n+1}(i,k) = & \frac{2\Delta t}{(2C_0\epsilon_x(i,k)+\Delta t\sigma_x^e(i,k))}\left(-\frac{\Delta H_y^{n+1/2}(i,k)}{\Delta z}\right) \\
& - \frac{2\Delta t}{(2C_0\epsilon_x(i,k)+\Delta t\sigma_x^e(i,k))}\sigma_x^e(i,k)\frac{E_x^n(i,k)}{2} \\
& - \frac{2\Delta t}{(2C_0\epsilon_x(i,k)+\Delta t\sigma_x^e(i,k))}J_{ix}^{n+1/2}(i,k) \\
& - \frac{2\epsilon_x(i,k)}{(2C_0\epsilon_x(i,k)+\Delta t\sigma_x^e(i,k))}\sum_{l=1}^{h} C_l\cdot E_x^{n+1-l}(i,k)
\end{aligned}
\tag{79}
$$

$$
\begin{aligned}
E_z^{n+1}(i,k) = & \frac{2\Delta t}{(2C_0\epsilon_z(i,k)+\Delta t\sigma_z^e(i,k))}\left(\frac{\Delta H_y^{n+1/2}(i,k)}{\Delta x}\right) \\
& - \frac{2\Delta t}{(2C_0\epsilon_z(i,k)+\Delta t\sigma_z^e(i,k))}\sigma_z^e(i,k)\frac{E_z^n(i,k)}{2} \\
& - \frac{2\Delta t}{(2C_0\epsilon_z(i,k)+\Delta t\sigma_z^e(i,k))}J_{iz}^{n+1/2}(i,k) \\
& - \frac{2\epsilon_z(i,k)}{(2C_0\epsilon_z(i,k)+\Delta t\sigma_z^e(i,k))}\sum_{l=1}^{h} C_l\cdot E_z^{n+1-l}(i,k)
\end{aligned}
\tag{80}
$$

$$
\begin{aligned}
H_x^{n+1/2}(i,k) = & \frac{2\Delta t}{(2C_0\mu_x(i,k)+\Delta t\sigma_x^m(i,k))}\left(\frac{\Delta E_y^n(i,k)}{\Delta z}\right) \\
& - \frac{2\Delta t}{(2C_0\mu_x(i,k)+\Delta t\sigma_x^m(i,k))}\sigma_x^m(i,k)\frac{H_x^{n-1/2}(i,k)}{2} \\
& - \frac{2\Delta t}{(2C_0\mu_x(i,k)+\Delta t\sigma_x^m(i,k))}M_{ix}^n(i,k) \\
& - \frac{2\mu_x(i,k)}{(2C_0\mu_x(i,k)+\Delta t\sigma_x^m(i,k))}\sum_{l=1}^{h} C_l \cdot H_x^{n+1/2-l}(i,k)
\end{aligned}
\tag{81}
$$

$$
\begin{aligned}
H_z^{n+1/2}(i,k) = & \frac{2\Delta t}{(2C_0\mu_z(i,k)+\Delta t\sigma_z^m(i,k))}\left(-\frac{\Delta E_y^n(i,k)}{\Delta x}\right) \\
& - \frac{2\Delta t}{(2C_0\mu_z(i,k)+\Delta t\sigma_z^m(i,k))}\sigma_z^m(i,k)\frac{H_z^{n-1/2}(i,k)}{2} \\
& - \frac{2\Delta t}{(2C_0\mu_z(i,k)+\Delta t\sigma_z^m(i,k))}M_{iz}^n(i,k) \\
& - \frac{2\mu_z(i,k)}{(2C_0\mu_z(i,k)+\Delta t\sigma_z^m(i,k))}\sum_{l=1}^{h} C_l \cdot H_z^{n+1/2-l}(i,k)
\end{aligned}
\tag{82}
$$

Using these updating equations the FDTD code updates first the H fields and then the E fields to complete a full propagation time step. In addition, to account for the current created in the plasma by the electric field, it is also necessary to have a current time stepping term which is derived in a similar way to the time stepping H fields as it is also calculated at half integer time steps.

The derivation starts with the equation for the force on an electron in an electromagnetic field from Equation 34 and as before neglect the presence of an external magnetic field and assume non-electron velocities to be negligible with respect to electrons velocities in order to get:

$$m_e \frac{\partial \boldsymbol{v}_e}{\partial t} = e\boldsymbol{E} + e\boldsymbol{v} \times \boldsymbol{B}_{external} - m_e \boldsymbol{v}_e \sum_s \nu_{es} \tag{83}$$

Next multiply both sides of this equation by $\frac{n_e}{m_e}$ and the electric charge e and substitute in the definition for the plasma frequency and the current density from Equation 33 as before to get:

$$\frac{\partial \boldsymbol{J}_e}{\partial t} = \epsilon_0 \omega_{pe}^2 \boldsymbol{E} + \frac{e}{m_e} \boldsymbol{J}_e \times \boldsymbol{B}_{external} - \boldsymbol{J}_e \sum_s \nu_{es} \tag{84}$$

or re-written in component form:

$$\frac{\partial J_x}{\partial t} = \epsilon_0 \omega_{pe}^2 E_x + \frac{e}{m_e}(J_y B_z - J_z B_y) - J_x \sum_s \nu_{es} \tag{85}$$

$$\frac{\partial J_y}{\partial t} = \epsilon_0 \omega_{pe}^2 E_y + \frac{e}{m_e}(J_z B_x - J_x B_z) - J_y \sum_s \nu_{es} \tag{86}$$

$$\frac{\partial J_z}{\partial t} = \epsilon_0 \omega_{pe}^2 E_z + \frac{e}{m_e}(J_x B_y - J_y B_x) - J_z \sum_s \nu_{es} \tag{87}$$

or solved for the components of J:

$$J_x = \frac{1}{\sum_s \nu_{es}(|B|^2 + (\sum_s \nu_{es})^2)} \Bigg[-((\sum_s \nu_{es})^2 - \frac{e^2 B_x^2}{m_e^2})(\frac{\partial J_x}{\partial t} - \epsilon_0 \omega_p^2 E_x) + (-\sum_s \nu_{es} \frac{eB_z}{m_e} - \frac{e^2 B_x B_y}{m_e^2})(\frac{\partial J_y}{\partial t} - \epsilon_0 \omega_p^2 E_y) + (\sum_s \nu_{es} \frac{eB_y}{m_e} - \frac{e^2 B_x B_z}{m_e^2})(\frac{\partial J_z}{\partial t} - \epsilon_0 \omega_p^2 E_z) \Bigg] \tag{88}$$

$$J_y = \frac{1}{\sum_s \nu_{es}(|B|^2 + (\sum_s \nu_{es})^2)} \Bigg[(\sum_s \nu_{es} \frac{eB_z}{m_e} - \frac{e^2 B_x B_y}{m_e^2})(\frac{\partial J_x}{\partial t} - \epsilon_0 \omega_p^2 E_x) + (-(\sum_s \nu_{es})^2 - \frac{e^2 B_y^2}{m_e^2})(\frac{\partial J_y}{\partial t} - \epsilon_0 \omega_p^2 E_y) + (-\sum_s \nu_{es} \frac{eB_x}{m_e} - \frac{e^2 B_y B_z}{m_e^2})(\frac{\partial J_z}{\partial t} - \epsilon_0 \omega_p^2 E_z) \Bigg] \tag{89}$$

$$\tag{90}$$

$$J_z = \frac{1}{\sum_s \nu_{es}(|B|^2 + (\sum_s \nu_{es})^2)} \Bigg[(-\sum_s \nu_{es} \frac{eB_y}{m_e} - \frac{e^2 B_x B_z}{m_e^2})(\frac{\partial J_x}{\partial t} - \epsilon_0 \omega_p^2 E_x) + (\sum_s \nu_{es} \frac{eB_z}{m_e} - \frac{e^2 B_y B_z}{m_e^2})(\frac{\partial J_y}{\partial t} - \epsilon_0 \omega_p^2 E_y) + (\frac{e^2 B_x^2}{m_e^2} + \frac{e^2 B_y^2}{m_e^2})(\frac{\partial J_z}{\partial t} - \epsilon_0 \omega_p^2 E_z) - \frac{1}{\sum_s \nu_{es}} \Bigg] \tag{91}$$

Similar to the E and H field equations, the J current density equation also needs to be discritized. The procedure for the y-component of the current density is shown for example, and the procedure and results for other current density components are analogous. Assuming that the external B field is negligible leaves:

$$\frac{C_0}{\Delta t} \cdot J_y^{n+1/2}(i,k) + \frac{1}{\Delta t} \sum_{l=1}^{h} C_l \cdot J_y^{n+1/2-l}(i,k) = \epsilon_0 \omega_{pe}^2 E_y^n(i,k) - J_y^n(i,k) \sum_s \nu_{es} \tag{92}$$

Similar to when discritizing the E field in Equation 69 since the equation needs J for the current time step it is estimated by averaging the values of the current at the previous half time step and the next half time step:

$$\frac{C_0}{\Delta t} \cdot J_y^{n+1/2}(i,k) + \frac{1}{\Delta t} \sum_{l=1}^{h} C_l \cdot J_y^{n+1/2-l}(i,k) = \epsilon_0 \omega_{pe}^2 E_y^n(i,k) - \frac{J_y^{n+1/2}(i,k) \sum_s \nu_{es} + J_y^{n-1/2}(i,k) \sum_s \nu_{es}}{2} \tag{93}$$

Subtract the sumation of the left hand side from both sides and multiply by Δt :

$$\begin{aligned} C_0 \cdot J_y^{n+1/2}(i,k) = {} & \Delta t \epsilon_0 \omega_{pe}^2 E_y^n(i,k) \\ & - \Delta t \frac{\left(J_y^{n+1/2}(i,k) \sum_s \nu_{es} + J_y^{n-1/2}(i,k) \sum_s \nu_{es} \right)}{2} \\ & - \sum_{l=1}^{h} C_l \cdot J_y^{n+1/2-l}(i,k) \end{aligned} \tag{94}$$

Take the $J_y^{n+1/2}$ term from the right and add it to the left side of the equation:

$$\left(C_0 + \frac{1}{2}\Delta t \sum_s \nu_{es}\right) \cdot J_y^{n+1/2}(i,k) = \Delta t \epsilon_0 \omega_{pe}^2 E_y^n(i,k) - \Delta t \frac{J_y^{n-1/2}(i,k) \sum_s \nu_{es}}{2} - \sum_{l=1}^{h} C_l \cdot J_y^{n+1/2-l}(i,k) \tag{95}$$

Finally solve for $J_y^{n+1/2}$ by dividing through:

$$J_y^{n+1/2}(i,k) = \frac{2\Delta t}{(2C_0 + \Delta t \sum_s \nu_{es})} \epsilon_0 \omega_{pe}^2 E_y^n(i,k) - \frac{2\Delta t}{(2C_0 + \Delta t \sum_s \nu_{es})} \frac{J_y^{n-1/2}(i,k) \sum_s \nu_{es}}{2} - \frac{2}{(2C_0 + \Delta t \sum_s \nu_{es})} \sum_{l=1}^{h} C_l \cdot J_y^{n+1/2-l}(i,k) \tag{96}$$

The solutions for J_x and J_z are the same except for their dependence on their respective electric fields.

With the time step propagation Equations 77 through 82 and 96 now derived it is important to note several considerations to take into account when modeling electromagnetic propagation with finite difference equations. The first is known as the Courant-Friedrichs-Lewy (CFL) condition which gives a necessary but not sufficient condition for convergence relating the time and distance steps for a grid, while using it to numerically solve a partial differential equation. On a 2D grid for FDTD propagation of an electromagnetic field the condition is given as [8, pg. 36]:

$$\Delta t \leq \frac{1}{c\sqrt{\frac{1}{(\Delta x)^2} + \frac{1}{(\Delta z)^2}}} \tag{97}$$

Another important consideration is that of numerical dispersion which can be illustrated in an example 1D case and then expanded to 2D by inspection. Let's begin with a 1D system of differential equations for electromagnetic field propagation which is governed by the following simplified Maxwell's Equations in free space [9, pg. 22]

$$\frac{\partial E_y(x,t)}{\partial t} = -\frac{1}{\epsilon}\frac{\partial H_z(x,t)}{\partial x} \tag{98}$$

$$\frac{\partial H_z(x,t)}{\partial t} = -\frac{1}{\mu}\frac{\partial E_y(x,t)}{\partial x} \tag{99}$$

These equations can be consolidated into the single wave equations for E_y:

$$\frac{\partial^2 E_y(x,t)}{\partial t^2} = c^2\frac{\partial^2 E_y(x,t)}{\partial x^2} \tag{100}$$

A solution to this equation takes the form:

$$E_y(x,t) = Ae^{j(\omega t - kx)} \tag{101}$$

Here $j = \sqrt{-1}$. The dispersion relation of a wave is defined as the equation which relates k the propagation vector to ω the wave frequency. It is obtained by plugging in the solution to both sides of the wave equation.

$$\frac{\partial^2}{\partial t^2} A e^{j(\omega t - kx)} = c^2 \frac{\partial^2}{\partial x^2} A e^{j(\omega t - kx)} \tag{102}$$

$$-\omega^2 A e^{j(\omega t - kx)} = -c^2 k^2 A e^{j(\omega t - kx)} \tag{103}$$

$$k = \pm \frac{\omega}{c} \tag{104}$$

To show how this analytic solution compares to the dispersion relationship obtained using numerical methods it will be repeated numerically below. First the wave solution is rewritten in discretized form where i and n are integer grid coordinates and Δx and Δt are the spacing in steps :

$$E_y(i, n) = A e^{j(\omega n \Delta t - ki\Delta x)} \tag{105}$$

Next the previously derived method in Equation 55 is used to numerically evaluate the differential equation using a second order central difference method:

$$\frac{\partial^2}{\partial t^2} A e^{j(\omega t - kx)} \approx \frac{A e^{j(\omega(n-1)\Delta t - ki\Delta x)} - 2 * A e^{j(\omega(n)\Delta t - ki\Delta x)} + A e^{j(\omega(n+1)\Delta t - ki\Delta x)}}{\Delta t^2} \tag{106}$$

$$\frac{\partial^2}{\partial x^2} A e^{j(\omega t - kx)} \approx \frac{A e^{j(\omega n \Delta t - k(i-1)\Delta x)} - 2 * A e^{j(\omega n \Delta t - k(i)\Delta x)} + A e^{j(\omega n \Delta t - k(i+1)\Delta x)}}{\Delta x^2} \tag{107}$$

These derivatives are substituted into the wave equation and like terms are removed from each side to get:

$$\frac{Ae^{-j\omega\Delta t} - 2 + Ae^{j\omega\Delta t}}{\Delta t^2} = c^2 \frac{Ae^{jk\Delta x} - 2 + Ae^{-jk\Delta x}}{\Delta x^2} \tag{108}$$

Which further simplifies:

$$\frac{Acos(\omega\Delta t) - 1}{\Delta t^2} = c^2 \frac{Acos(k\Delta x) - 1}{\Delta x^2} \tag{109}$$

$$k = \frac{1}{\Delta x} cos^{-1}\left(\frac{\Delta x^2(Acos(\omega\Delta t) - 1)}{c^2\Delta t^2} + 1\right) \tag{110}$$

Notice that this equation is distinct from the analytic dispersion relation derived without discretization but reduces to the analytic solution for small values of $k\Delta x$ and $\omega\Delta t$. This matches intuition as with infinitesimally fine grid spacing the approximation becomes equal to the analytic solution.

2.5 Absorbing Boundary Conditions

Often in simulations it is desirable to simulate objects as free standing in space. One method to accomplish this is through the use of analytic boundary conditions at the edge of the simulation grid which absorb outgoing waves as if they continue into free space. Enquist and Mahjda showed that the standard 2D wave equation could be factored into a left propagating and right propagating wave equation and then used this observation to create perfectly absorbing boundary conditions [10]. This derivation is recreated below for the 2D wave equation in the x-z plane which is given by:

$$\left(\frac{\partial^2}{\partial x^2} + \frac{\partial^2}{\partial z^2} - \frac{1}{c^2}\frac{\partial^2}{\partial t^2}\right) U = 0 \tag{111}$$

To ease manipulation of the differential operators they are written more compactly as:

$$\frac{\partial^2}{\partial x^2} = D_x^2 \tag{112}$$

$$\frac{\partial^2}{\partial z^2} = D_z^2 \tag{113}$$

$$\frac{\partial^2}{\partial t^2} = D_t^2 \tag{114}$$

and the wave equation becomes:

$$\left(D_x^2 + D_z^2 - \frac{1}{c^2}D_t^2\right) U = 0 \tag{115}$$

The differential operator term can then be factored as:

$$\left(D_x + \frac{1}{c}D_t\sqrt{1 - c^2\frac{D_z^2}{D_t^2}}\right)\left(D_x - \frac{1}{c}D_t\sqrt{1 - c^2\frac{D_z^2}{D_t^2}}\right) U = 0 \tag{116}$$

Enquist and Mahjda then showed that at the boundaries of x using each of the 'factors' results in perfectly absorbing boundary conditions at $x = 0$ and $x = h$:

$$\left(D_x - \frac{1}{c}D_t\sqrt{1 - c^2\frac{D_z^2}{D_t^2}}\right)U|_{x=0} = 0 \tag{117}$$

$$\left(D_x + \frac{1}{c}D_t\sqrt{1 - c^2\frac{D_z^2}{D_t^2}}\right)U|_{x=h} = 0 \tag{118}$$

However the square root of the differential operators is not well defined and can't easily be implemented into discrete code. In order to approximate this differential equation the square root term can be replaced with its Taylor series truncated at the desired order of accuracy. The Taylor series of the square root function up to the second order term is given as:

$$\sqrt{1 - s^2} = 1 - \frac{s^2}{2} + O(s^3) \tag{119}$$

Using this substitution for the square root term the absorbing boundary conditions become:

$$\left(D_x - \frac{1}{c}D_t + \frac{c}{2}\frac{D_z^2}{D_t}\right)U|_{x=0} = 0 \tag{120}$$

$$\left(D_x + \frac{1}{c}D_t - \frac{c}{2}\frac{D_z^2}{D_t}\right)U|_{x=h} = 0 \tag{121}$$

Multiplying by a factor of D_t to remove it from the denominator in the third term yields the second order equations for 2D absorbing boundary conditions:

$$\left(D_t D_x - \frac{1}{c} D_t^2 + \frac{c}{2} D_z^2\right) U|_{x=0} = 0 \tag{122}$$

$$\left(D_t D_x + \frac{1}{c} D_t^2 - \frac{c}{2} D_z^2\right) U|_{x=h} = 0 \tag{123}$$

Using these boundary conditions for the y component of an electric field on a x-z grid yields:

$$\frac{\partial^2 E_y}{\partial t \partial x}|_{x=0} - \frac{1}{c}\frac{\partial^2 E_y}{\partial t^2}|_{x=0} + \frac{c}{2}\frac{\partial^2 E_y}{\partial z^2}|_{x=0} = 0 \tag{124}$$

$$\frac{\partial^2 E_y}{\partial t \partial x}|_{x=h} + \frac{1}{c}\frac{\partial^2 E_y}{\partial t^2}|_{x=h} - \frac{c}{2}\frac{\partial^2 E_y}{\partial z^2}|_{x=h} = 0 \tag{125}$$

$$\frac{\partial^2 E_y}{\partial t \partial z}|_{z=0} - \frac{1}{c}\frac{\partial^2 E_y}{\partial t^2}|_{z=0} + \frac{c}{2}\frac{\partial^2 E_y}{\partial x^2}|_{z=0} = 0 \tag{126}$$

$$\frac{\partial^2 E_y}{\partial t \partial z}|_{z=h} + \frac{1}{c}\frac{\partial^2 E_y}{\partial t^2}|_{z=h} - \frac{c}{2}\frac{\partial^2 E_y}{\partial x^2}|_{z=h} = 0 \tag{127}$$

Mur points out that in the 2D case of free space propagation spacial derivatives with respect to the E field can be replaced with time derivatives with respect to the H field in free space by using Maxwell's equations, specifically by rearranging Equations 59 and 61 without the conductivity and current terms [11]:

$$\frac{\partial E_y}{\partial z} = \mu_x \frac{\partial H_x}{\partial t} \tag{128}$$

$$\frac{\partial E_y}{\partial x} = -\mu_z \frac{\partial H_z}{\partial t} \tag{129}$$

Equations 128 and 129 are substituted into equations 124 through 127 to obtain:

$$\frac{\partial^2 E_y}{\partial t \partial x}|_{x=0} - \frac{1}{c}\frac{\partial^2 E_y}{\partial t^2}|_{x=0} + \frac{\mu_x c}{2}\frac{\partial^2 H_x}{\partial z \partial t}|_{x=0} = 0 \tag{130}$$

$$\frac{\partial^2 E_y}{\partial t \partial x}|_{x=h} + \frac{1}{c}\frac{\partial^2 E_y}{\partial t^2}|_{x=h} - \frac{\mu_x c}{2}\frac{\partial^2 H_x}{\partial z \partial t}|_{x=h} = 0 \tag{131}$$

$$\frac{\partial^2 E_y}{\partial t \partial z}|_{z=0} - \frac{1}{c}\frac{\partial^2 E_y}{\partial t^2}|_{z=0} - \frac{\mu_z c}{2}\frac{\partial^2 H_z}{\partial x \partial t}|_{z=0} = 0 \tag{132}$$

$$\frac{\partial^2 E_y}{\partial t \partial z}|_{z=h} + \frac{1}{c}\frac{\partial^2 E_y}{\partial t^2}|_{z=h} + \frac{\mu_z c}{2}\frac{\partial^2 H_z}{\partial x \partial t}|_{z=h} = 0 \tag{133}$$

These equations can then be integrated with respect to time and the resulting arbitrary constant can be set to zero so that the boundary equations only require first derivatives and finally obtain Mur's second order accurate first derivative boundary conditions:

$$\frac{\partial E_y}{\partial x}|_{x=0} - \frac{1}{c}\frac{\partial E_y}{\partial t}|_{x=0} + \frac{\mu_x c}{2}\frac{\partial H_x}{\partial z}|_{x=0} = 0 \tag{134}$$

$$\frac{\partial E_y}{\partial x}|_{x=h} + \frac{1}{c}\frac{\partial E_y}{\partial t}|_{x=h} - \frac{\mu_x c}{2}\frac{\partial H_x}{\partial z}|_{x=h} = 0 \tag{135}$$

$$\frac{\partial E_y}{\partial z}|_{z=0} - \frac{1}{c}\frac{\partial E_y}{\partial t}|_{z=0} - \frac{\mu_z c}{2}\frac{\partial H_z}{\partial x}|_{z=0} = 0 \tag{136}$$

$$\frac{\partial E_y}{\partial z}|_{z=h} + \frac{1}{c}\frac{\partial E_y}{\partial t}|_{z=h} + \frac{\mu_z c}{2}\frac{\partial H_z}{\partial x}|_{z=h} = 0 \tag{137}$$

These are the boundary conditions that are discritized and used in the FDTD simulation.

2.6 Near-Field to Far-Field Transformation

By definition the RCS of an object is calculated using the reflected field far from the object. Close to the object higher order fields may be created however far away from the object these fields will decay and become irrelevant for RCS calculations.

To determine the far-field reflection of the incident electromagnetic wave it is not necessary to extend the computational grid into the far field from the scattering object. Instead several methods have been developed to transform the scattered near-field wave to the far-field form using what is known as a near-field to far-field transformation. Taflove in his textbook "Computational Electrodynamics, The Finite Difference Time Domain" provides an examples of the proof of such a transform using Green's theorem and will be recreated in this section [9].

The near to far field transform uses Green's theorem applied to a surface which is created by a square surface around the scattering object that is infinitesimally connected by a thin strip to an infinitely far away surface circularly symmetric in the far field as shown in Figure 6.

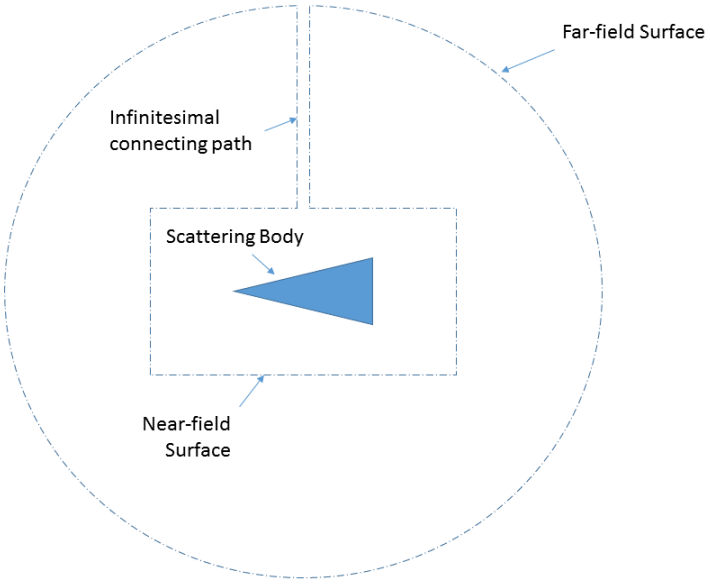

Figure 6. Diagram showing the integration surface for using Green's Theorem to calculate a Near-Field to Far-Field Transform

Applying Green's theorem to the y component of the electric field gives:

$$\int_S \left[\tilde{E}_y(\boldsymbol{r}')(\nabla^2)'G(\boldsymbol{r}|\boldsymbol{r}') - G(\boldsymbol{r}|\boldsymbol{r}')(\nabla^2)'\tilde{E}_y(\boldsymbol{r}')\right] ds' \\ = \oint_{C_\infty} \left[\tilde{E}_y(\boldsymbol{r}')\frac{\partial G(\boldsymbol{r}|\boldsymbol{r}')}{\partial r'} - G(\boldsymbol{r}|\boldsymbol{r}')\frac{\partial \tilde{E}_y(\boldsymbol{r}')}{\partial r'}\right] dC' \\ - \oint_{C_a} \left[\tilde{E}_y(\boldsymbol{r}')\frac{\partial G(\boldsymbol{r}|\boldsymbol{r}')}{\partial n'_a} - G(\boldsymbol{r}|\boldsymbol{r}')\frac{\partial \tilde{E}_y(\boldsymbol{r}')}{\partial n'_a}\right] dC' \tag{138}$$

here G is the Green's Function in two dimensional space, C_a is the square path around the radiating object, and C_∞ is a circular path around the object infinitely far away which is in the far-field. Since both $\tilde{E}$ and G decay as $1/\sqrt{r'}$ in two dimensions the contour integral at the far-field surface goes to zero and the equation reduces to:

$$\int_S \left[\tilde{E}_y(\boldsymbol{r}')(\nabla^2)'G(\boldsymbol{r}|\boldsymbol{r}') - G(\boldsymbol{r}|\boldsymbol{r}')(\nabla^2)'\tilde{E}_y(\boldsymbol{r}')\right] ds' \\ = -\oint_{C_a} \left[\tilde{E}_y(\boldsymbol{r}')\frac{\partial G(\boldsymbol{r}|\boldsymbol{r}')}{\partial n'_a} - G(\boldsymbol{r}|\boldsymbol{r}')\frac{\partial \tilde{E}_y(\boldsymbol{r}')}{\partial n'_a}\right] dC' \tag{139}$$

The laplacian of $\tilde{E}$ is fairly simple in Fourier space and G is found using the definition of Green's function for a time harmonic series:

$$(\nabla^2)'G(\boldsymbol{r}|\boldsymbol{r}') = \delta(\boldsymbol{r}-\boldsymbol{r}') - k^2 G(\boldsymbol{r}|\boldsymbol{r}') \tag{140}$$

$$(\nabla^2)'\tilde{E}_y(\boldsymbol{r}') = -k^2\tilde{E}_y(\boldsymbol{r}') \tag{141}$$

Equation 139 now becomes:

$$\int_S \left(\tilde{E}_y(\boldsymbol{r}') \left[\delta(\boldsymbol{r} - \boldsymbol{r}') - k^2 G(\boldsymbol{r}|\boldsymbol{r}') \right] + G(\boldsymbol{r}|\boldsymbol{r}') k^2 \tilde{E}_y(\boldsymbol{r}') \right) ds' \\ = - \oint_{C_a} \left[\tilde{E}_y(\boldsymbol{r}') \frac{\partial G(\boldsymbol{r}|\boldsymbol{r}')}{\partial n'_a} - G(\boldsymbol{r}|\boldsymbol{r}') \frac{\partial \tilde{E}_y(\boldsymbol{r}')}{\partial n'_a} \right] dC' \tag{142}$$

The positive and negative product of $k^2 \tilde{E}_y$ and G cancel in the integral over S and the derivatives normal to the inner path are generalized to directional gradients aligned with the path normal to obtain:

$$\int_S \tilde{E}_y(\boldsymbol{r}') \delta(\boldsymbol{r} - \boldsymbol{r}') ds' = \tilde{E}_y(\boldsymbol{r}) = - \oint_{C_a} \left[\tilde{E}_y(\boldsymbol{r}') \hat{\boldsymbol{n}}'_a \cdot \boldsymbol{\nabla}' G(\boldsymbol{r}|\boldsymbol{r}') - G(\boldsymbol{r}|\boldsymbol{r}') \hat{\boldsymbol{n}}'_a \cdot \boldsymbol{\nabla}' \tilde{E}_y(\boldsymbol{r}') \right] dC' \tag{143}$$

In two dimensions the Green's function for time harmonic systems is given as:

$$G(\boldsymbol{r}|\boldsymbol{r}') = \frac{j}{4} H_0^{(2)}(k|\boldsymbol{r} - \boldsymbol{r}'|) \tag{144}$$

Where $H_0^{(2)}$ is the Hankel function of the second kind. If it is assumed that $\boldsymbol{r}$ is much larger than $\boldsymbol{r}'$ this G has the limit as it approaches infinity of:

$$\lim_{k|\boldsymbol{r} - \boldsymbol{r}'| \to \infty} G(\boldsymbol{r}|\boldsymbol{r}') = \frac{j^{3/2} e^{-jkr}}{\sqrt{8\pi kr}} e^{jk\hat{\boldsymbol{r}} \cdot \boldsymbol{r}'} \tag{145}$$

Taking the gradient of this expression gives:

$$\lim_{k|\boldsymbol{r}-\boldsymbol{r}'|\to\infty} \boldsymbol{\nabla}' G(\boldsymbol{r}|\boldsymbol{r}') = (jk\hat{\boldsymbol{r}})\frac{j^{3/2}e^{-jkr}}{\sqrt{8\pi kr}} e^{jk\hat{\boldsymbol{r}}\cdot\boldsymbol{r}'} \tag{146}$$

Using these limiting expressions for G in Equation 143 gives:

$$\begin{aligned}\tilde{E}_y(\boldsymbol{r}) = &\frac{j^{3/2}e^{-jkr}}{\sqrt{8\pi kr}} \oint_{C_a} \nabla\tilde{E}_y(\boldsymbol{r}') \cdot e^{jk\hat{\boldsymbol{r}}\cdot\boldsymbol{r}'}\hat{\boldsymbol{n}}'_a dC' \\ &- \frac{j^{3/2}e^{-jkr}}{\sqrt{8\pi kr}} \oint_{C_a} (jk\hat{\boldsymbol{r}})e^{jk\hat{\boldsymbol{r}}\cdot\boldsymbol{r}'} \cdot \tilde{E}_y(\boldsymbol{r}')\hat{\boldsymbol{n}}'_a dC'\end{aligned} \tag{147}$$

Equation 147 can be further simplified by factoring out a term and combining the path integrals:

$$\tilde{E}_y(\boldsymbol{r}) = \frac{j^{3/2}e^{-jkr}}{\sqrt{8\pi kr}} \oint_{C_a} \left[\hat{\boldsymbol{n}}'_a \cdot \boldsymbol{\nabla}'\tilde{E}_y(\boldsymbol{r}) - jk\tilde{E}_y(\boldsymbol{r})\hat{\boldsymbol{n}}'_a \cdot \hat{\boldsymbol{r}}'\right] e^{jk\hat{\boldsymbol{r}}\cdot\boldsymbol{r}} dC' \tag{148}$$

Next, the gradient of $\tilde{E}$ is expanded in the Cartesian coordinate system that aligns with the interior path integral since it is a square:

$$\boldsymbol{\nabla}'\tilde{E}(\boldsymbol{r}') = \hat{\boldsymbol{x}}'\frac{\partial\tilde{E}_y}{\partial x'} + \hat{\boldsymbol{z}}'\frac{\partial\tilde{E}_y}{\partial z'} \tag{149}$$

These derivatives of $\tilde{E}_y$ can be replaced using Maxwell's equations with the time harmonic derivatives of $\tilde{\boldsymbol{H}}$ so the equation becomes:

$$\boldsymbol{\nabla}'\tilde{E}(\boldsymbol{r}') = \hat{\boldsymbol{x}}'(j\omega\mu_0\tilde{H}_z) + \hat{\boldsymbol{z}}'(-j\omega\mu_0\tilde{H}_x) = -j\omega\mu_0\hat{\boldsymbol{y}}' \times \tilde{\boldsymbol{H}}(\boldsymbol{r}') \tag{150}$$

Dotting $\hat{\boldsymbol{n}}'_a$ to both sides of Equation 150 yields:

$$\hat{\boldsymbol{n}}'_a \cdot \boldsymbol{\nabla}' \tilde{E}(\boldsymbol{r}') = -j\omega\mu_0 \hat{\boldsymbol{n}}'_a \cdot \left[\hat{\boldsymbol{y}}' \times \tilde{\boldsymbol{H}}(\boldsymbol{r}')\right] = j\omega\mu_0 \hat{\boldsymbol{y}}' \cdot \left[\hat{\boldsymbol{n}}'_a \times \tilde{\boldsymbol{H}}(\boldsymbol{r}')\right] \tag{151}$$

The second term on the right hand side of Equation 148 can be rewritten in a similar way using a vector identity:

$$\hat{\boldsymbol{n}}'_a(\hat{\boldsymbol{y}}' \cdot \tilde{\boldsymbol{E}}(\boldsymbol{r}')) \cdot \hat{\boldsymbol{r}} - \tilde{\boldsymbol{E}}(\boldsymbol{r}')(\hat{\boldsymbol{y}}' \cdot \hat{\boldsymbol{n}}'_a) \cdot \hat{\boldsymbol{r}} = \left(\hat{\boldsymbol{y}}' \times \left[\hat{\boldsymbol{n}}'_a \times \tilde{\boldsymbol{E}}(\boldsymbol{r}')\right]\right) \cdot \hat{\boldsymbol{r}} \tag{152}$$

$$\tilde{E}_y(\boldsymbol{r}')\hat{\boldsymbol{n}}'_a \cdot \hat{\boldsymbol{r}} = \left(\hat{\boldsymbol{y}}' \times \left[\hat{\boldsymbol{n}}'_a \times \tilde{\boldsymbol{E}}(\boldsymbol{r}')\right]\right) \cdot \hat{\boldsymbol{r}} \tag{153}$$

Substituting in the terms from Equations 151 and 153 into Equation 148 yields

$$\tilde{E}_y(\boldsymbol{r}) = \frac{j^{3/2}e^{-jkr}}{\sqrt{8\pi kr}} \oint_{C_a} \left[j\omega\mu_0 \hat{\boldsymbol{y}}' \cdot \left[\hat{\boldsymbol{n}}'_a \times \tilde{\boldsymbol{H}}(\boldsymbol{r}')\right] - jk\left(\hat{\boldsymbol{y}}' \times \left[\hat{\boldsymbol{n}}'_a \times \tilde{\boldsymbol{E}}(\boldsymbol{r}')\right]\right) \cdot \hat{\boldsymbol{r}}\right] e^{jk\hat{\boldsymbol{r}}\cdot\boldsymbol{r}'} dC' \tag{154}$$

This equation can be rewritten in terms of phasor tangential equivalent currents yielding:

$$\tilde{\boldsymbol{J}}_{eq}(\boldsymbol{r}') = \hat{\boldsymbol{n}}_a \times \tilde{\boldsymbol{H}} \tag{155}$$

$$\tilde{\boldsymbol{M}}_{eq}(\boldsymbol{r}') = -\hat{\boldsymbol{n}}_a \times \tilde{\boldsymbol{E}} \tag{156}$$

$$\tilde{E}_y(\boldsymbol{r}) = \frac{j^{5/2}e^{-jkr}}{\sqrt{8\pi kr}} \oint_{C_a} \left[\omega\mu_0 \hat{\boldsymbol{y}}' \cdot \tilde{\boldsymbol{J}}_{eq}(\boldsymbol{r}') + k\hat{\boldsymbol{y}}' \times \tilde{\boldsymbol{M}}_{eq}(\boldsymbol{r}') \cdot \hat{\boldsymbol{r}}\right] e^{jk\hat{\boldsymbol{r}}\cdot\boldsymbol{r}'} dC' \tag{157}$$

The radar cross section in the far field is simply this term without the radial decay

terms sometimes known as the pattern function $F(\phi)$ compared to the incident E field times 2π radians:

$$F(\phi) = j^{5/2} \oint_{C_a} \left[\omega \mu_0 \hat{\boldsymbol{y}}' \cdot \tilde{\boldsymbol{J}}_{eq}(\boldsymbol{r}') + k \hat{\boldsymbol{y}}' \times \tilde{\boldsymbol{M}}_{eq}(\boldsymbol{r}') \cdot \hat{\boldsymbol{r}} \right] e^{jk\hat{\boldsymbol{r}} \cdot \boldsymbol{r}'} dC' \tag{158}$$

$$RCS\phi = \frac{\text{power scattered per unit angle in direction } \hat{\boldsymbol{r}}}{\text{incident power per unit length}} = 2\pi \frac{|F(\phi)|^2}{|\tilde{\boldsymbol{E}}_{inc}|^2} \tag{159}$$

III. Methodology

The approach taken to numerically simulate the effect of hypersonic plasma sheaths on a basic vehicle's radar cross section relies on two simulation steps. First a basic vehicle profile was generated in LAURA and the surrounding atmospheric environment was simulated for nine hypersonic flight conditions by the computational code. This simulation had a large number of outputs, the main ones of interest consisted of the plasma and neutral temperatures, neutral molecular number densities, as well as ion and electron number densities. Since the calculations were done for an axially symmetric body they are valid for any planar slice containing the axis, this allows the FDTD computation to be simplified and run in 2D. For the second simulation these outputs are used to calculate a conductivity that represents the plasma and is used in a numerical FDTD code written in MATLAB. This MATLAB code sends an electromagnetic wave at the hypersonic vehicle and calculates the near field electromagnetic scattering. A near-field to far-field transformation step is preformed to obtain the final radar cross section of the hypersonic vehicle. This procedure is preformed both with the plasma conductivity and without it to compare the effect is has on the vehicles RCS.

3.1 LAURA Simulations

Langley Aerothermodynamic Upwind Relaxation Algorithm (LAURA) is a structured simulation code maintained by NASA for the modeling of hypersonic flows around aerobodies [12]. For this project version 5.5 of the code was run on a Linux system using a command line interface with several input files specifying parameters. The output data from the code was originally saved into several files (*.g, *.q, *.nam) that are opened with the Tecplot 360 program. Once opened in Tecplot 360 these

files were exported into a standard text format that could be read into MATLAB for plotting and incorporation into the electromagnetic FDTD code. There were three air density and temperature pairs that correspond to a set of three altitudes in the atmosphere each run at three speeds for a total of nine condition profiles. The values for these parameters are specified in Table 3.

Table 3. Atmospheric Conditions used for LAURA Simulations

Altitude (km)	Temperature (K)	Density (kg/m^3)	Air Speed (km/s)
40	251	3.85e-03	5, 6, 7
60	245	2.88e-04	5, 6, 7
80	197	1.57e-05	5, 6, 7

A complete example of the namelist file that LAURA uses to initialize its simulation run and the explanation of the specified parameters are available in the Appendix A.

In these nine simulations several approximations were used to simplify the problem. The calculations did not account for turbulence, radiative heat transfer, or ablation. The effect of turbulence is to increase the effective viscosity of the fluid which increases energy diffusion. Leaving this term out may lead to steeper energy gradients. Radiative heat transfer is only relevant at very high temperature low speed flows since it is proportional to the fourth power of temperature. A lower temperatures it quickly becomes negligible. Ablation is the breaking/burning off of material from the hypersonic body's surface, in many applications it is intentionally done to remove heat from the surface. The main effects of ablation that are relevant for consideration in the analysis are the introduction of new chemical species derived from the surface material of the body, usually carbon based. These additional chemicals have the potential to alter the plasma parameters by adding additional chemical species which have higher or lower ionization energies. However if the concentration of this material is assumed to be low the effect should be negligible. Also the boundary condition at the vehicles surface was treated as 'super-catalytic' meaning that the simulation

reverted all species to their free stream mass fractions at the surface of the aerobody. Four additional simulations were run for 80 km altitude at 6 km/s and 5 km/s, and one at 60 km altitude at 5 km/s. These additional simulations used LAURA's Menter-SST two-equation turbulence model as well as an 'equilibrium-catalytic' boundary condition at the aerobodies surface meaning that the mass fractions of the species at the surface were determined to be equal to those one grid above the surface. Those more complex phenomena were modeled for these four conditions specifically because they had lower particle densities and would be the much more highly impacted by the simplifications used in the other cases.

The modeled hypersonic cone was specified to have a 6-degree half angle, a length of 3.5 meters, and a blunted nose with a circular radius of 2.5 centimeters. The modeling grid had 128 cells along the symmetry plane, 20 axial direction cells on the cap, and initially 16 cells outward from the surface which was doubled a total of three times after sufficient convergence criteria (L2 norm of less than 10^{-2}) before obtaining total convergence with 128 cells outward from the body surface. Two images showing the final mesh configuration are shown in Figures 7 and 8.

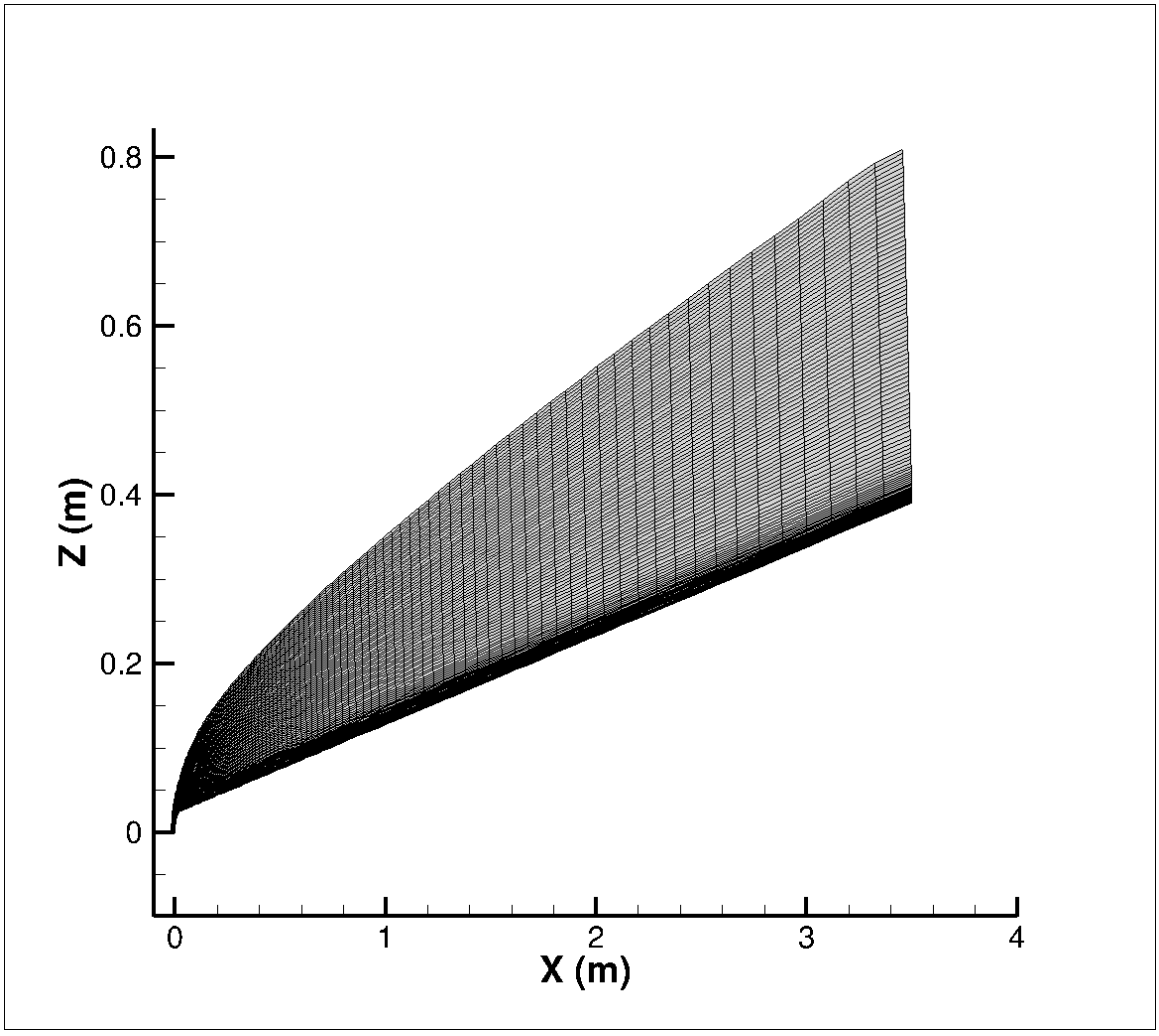

Figure 7. Example of the mesh used for LAURA hypersonic simulations

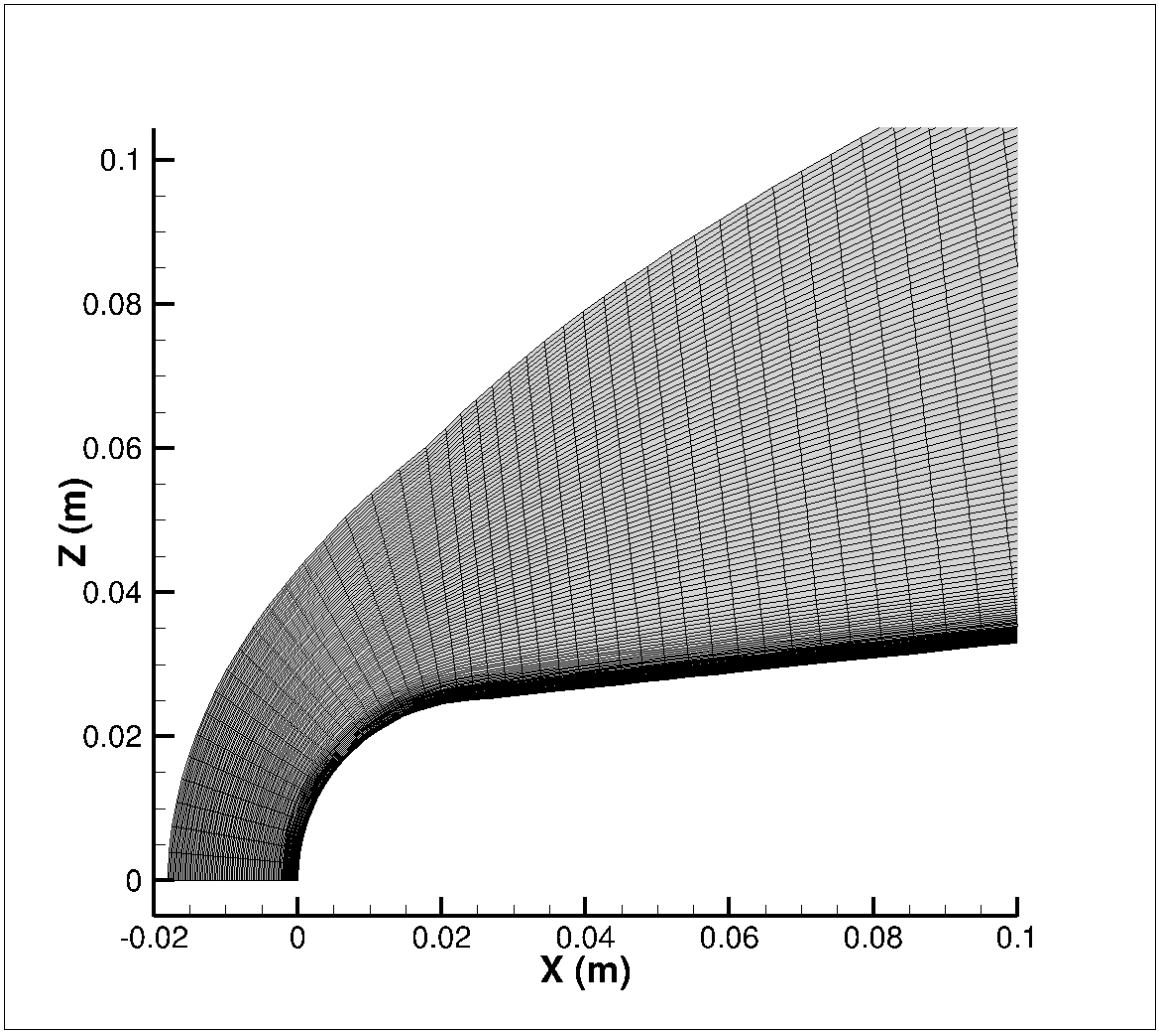

Figure 8. Zoomed in view of Figure 7, the mesh used for LAURA hypersonic simulations

The approach for obtaining a converged solution starts with a similar method to that used in the LAURA 5.5 manual and is summarized in Table 4 [13, pg. 68-73]. Total convergence of the simulation was determined by achieving an L2 norm of less than 10^{-10} in most cases, or an L2 norm of less than 10^{-8} if more than 20,000 iterations had taken place in the final convergence run.

Table 4. Summary of basic procedural runs in LAURA used to obtain convergence

Run	Summary of Procedure
1	Run 2000 iterations with 1500 1st order relaxation steps
2	Run with implicit true until 16 initial k direction cells, double 4 times to 128 final k direction cells, align shock every 2000 iterations up to 3 times
3	Set implicit to false for 'faster' convergence run until L2 Norm $< 10^{-10}$ or $>$ 20,000 iterations, align shock every 2000 iterations up to 3 times
4 (if not converged)	Switch back to implicit true and run with same exit criteria as the 3rd run, align shock every 2000 iterations up to 3 times
5 (if not converged)	Switch back to implicit false with the same exit criteria as 3rd and 4th runs.

3.2 Implimenting FDTD Code for RCS Calculation

The Finite Difference Time Domain (FDTD) method is one of the most common methods used to calculate the radar cross section of objects and has a number of potential advantages. One advantage of this methods is the ability to watch the wave interact and travel in real time as it propagates through the environment, this can aid in the understanding of how the end results of the propagation is obtained. Another advantage is, in contrast to a frequency domain propagation, multiple frequency and wave forms can be tested in a single simulation. If the effects on a specific frequency are desired they can be obtained through a Fourier Transform of the input and output. One noted disadvantage is the occurrence of numerical dispersion which artificially increases the dispersion of a wave being propagated due to the the discretization of the differential equations [9, pg. 107]. An FDTD MATLAB code was written for this study to enable control over transference and implementation of the data obtained from the LAURA hypersonic simulation into the electromagnetic

propagation code. The FDTD MATLAB code implementation used in this study has three main components, the main propagation code which handles initial radiation source and propagation of the electromagnetic wave, the numerical absorbing boundary conditions which allow approximation of an isolated system in free space, and the extrapolation of the reflected waves to far-field to calculate the far-field radar cross section.

The main propagation code implementation was the use of a Yee grid with staggered electric and magnetic field components as previously discussed in Section 2.4. The Yee grid allows for second order numerical accuracy while saving data storage space since the staggered field components allow for an effective grid twice as fine as a standard implementation. Due to it's relative simplicity and high accuracy, Yee's implementation is one of the most long lasting and common FDTD implementations [9, pg. 51].

The presence of the plasma sheath around the hypersonic vehicle is incorporated into the propagation by defining a plasma current based upon the calculated plasma frequency as well as the electron-ion and electron-neutral collision frequencies as shown in Section 2.4. However at higher plasma frequencies the implementation of Equation 96 becomes problematic because the increase in the plasma current over a single time step can no longer be considered linear. One solution to this problem is to choose a time step small enough over which the increase in current is slow enough that it can be considered linear, unfortunately for the high plasma frequencies in this study the time step needed to do this is several orders of magnitude smaller than would other wise would be needed and would therefor increase the run time of the simulation proportionally. A second solution to this problem is to recognize that rather than increasing linearly over an entire time step the current will stop rising when its derivative becomes zero and the current can be said to be in equilibrium.

This equilibrium value can be found as the solution to the Equation 84 (again ignoring an external magnetic field) where the derivative of J is zero, or simply:

$$\boldsymbol{J_e} = \frac{\epsilon_0 \omega_{pe}^2 \boldsymbol{E}}{\nu_{es}} \tag{160}$$

This allows the plasma current to be represented with a constant scalar conductivity if the plasma frequency becomes too high to properly simulate with the relatively course time steps. Also the nature of the way in which the conductivity is implemented in Equation 77 ensures that the self-influence of the plasma current on the E field is still properly taken into account.

A second consideration when implementing the FDTD code is the scaling detail needed to properly represent the thin plasma sheath. In order to increase the resolution of the grid without drastically increasing computational time a technique called frequency scaling was used. The theory of frequency scaling is that if the ratio between an object's length scale and incident wavelength is held constant the scattering response of the electromagnetic wave will be the same [14]. This technique allows the nose of the blunted cone to be simulated as 10x larger by irradiating it with a wavelength also 10x larger, which means a frequency 10x smaller than that for which the response is to simulated. The enlarged blunted cone has a tip radius of 25 cm instead of 2.5 cm and a full scaled length of 35 m. However the wake region and trailing effects of the plasma sheath were outside the scope of this study and only the first 1/10th of the cone is simulated to calculate the effects of the plasma sheath (which is also scaled in size) on the cone's radar cross section. The calculated collision and plasma frequencies from the LAURA output are transferred onto the FDTD grid by taking their values at the closest known point in space in the LAURA output at each point in the FDTD grid. The conductivity of the vehicle itself is calculated using a

Drude fit of the collision and plasma frequencies for titanium, $\nu = 1.146 \times 10^{13}$ Hz, $\omega_p = 6.09 \times 10^{14}$ Hz, which is a major metallurgical component of the SR-71 and was a sufficient generic conductivity for the purposes of this study [15].

The implementation of highly absorbing boundary conditions in the code utilizes a second order finite difference formulation described by Mur [11] and reproduced in Section 2.5. Mur applied the discretized analytic absorbing boundary conditions derived from the one way wave equations in [10] to the Yee propagation method for electromagnetic waves. These highly absorbing boundary conditions are necessary to attenuate the reflection of the reflected waves at the boundaries of the simulation so that an equilibrium solution can be obtained for the radar reflection and the far-field extrapolation of the reflected field can be calculated.

The near-to-far-field transform of the reflected wave uses the surface equivalence theorem and Green's Theorem to calculate the reflected far-field electric and magnetic fields at an arbitrary location in space [9, pg. 329]. The transform integrates the magnetic and electric fields along an arbitrary virtual surface to obtain equivalent electric and magnetic current sources which represent the source of the original fields, the derivation of this is reproduced in Section 2.6. Using these new current sources with Green's Theorem allows for the calculation of the electric and magnetic fields anywhere in space. By calculating these fields at a distance in the far-field they can then be used to determine the reflected energy for a total bistatic RCS calculation. A diagram showing the layout of the NTFF boundary and other considerations in the simulation space is shown in Figure 9.

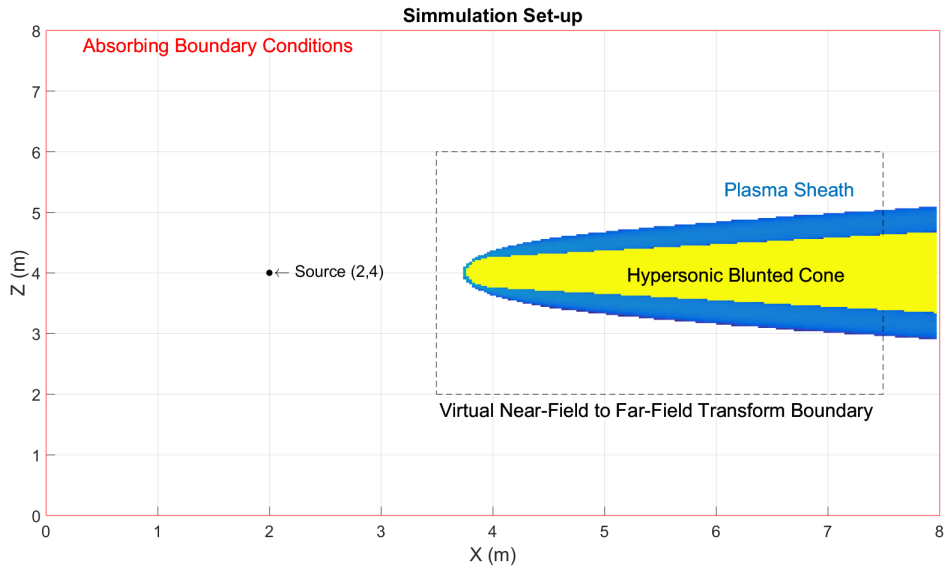

Figure 9. Diagram showing the set-up of the simulation space

The electromagnetic field source in the FDTD simulation is a "soft" sinusoidal line current surrounded by free space flowing in the y direction with a frequency of 3 MHz. This oscillating current creates a TM cylindrical wave which propagates through the E_y, H_x, and H_z fields. The term "soft" indicates that the current was not directly specified at that point, instead it was calculated as an additive $J_i y^{n+1/2}$ term in Equation 77. This source term is positioned at a point (2,4) as shown in Figure 9 which is 3 scaled meters from the center of the cone's circular nose tip. The source current was run continuously, steady state equilibrium within the simulation space was reached as designated by the total relative change in energy being less than 0.1% from the energy calculated after the previous wavelength. In order to calculate the energy field in the simulation space at exactly the same phase from the source the time step was decreased as necessary so that its product with the frequency would be an integer value. After an equilibrium state was reached the source irradiation was continued for two subsequent wavelength cycles while the electric and magnetic fields were recorded along the NTFF boundary to preform the NTFF transformation

discussed in Section 2.6

In order to verify the physical validity of the code a bistatic radar cross section for a conducting square with sides one meter in length was calculated at a frequency of 600 MHz using a sine wave current source in the y direction. The source creates a cylindrical wave and was 16.1 meters from the conducting square which was oriented with one of its corners directly facing the source. The source was placed far from the square to better approximate an incoming plane wave which was the source used in the reference paper used to compare against [14]. A set-up diagram for this case is shown in Figure 10.

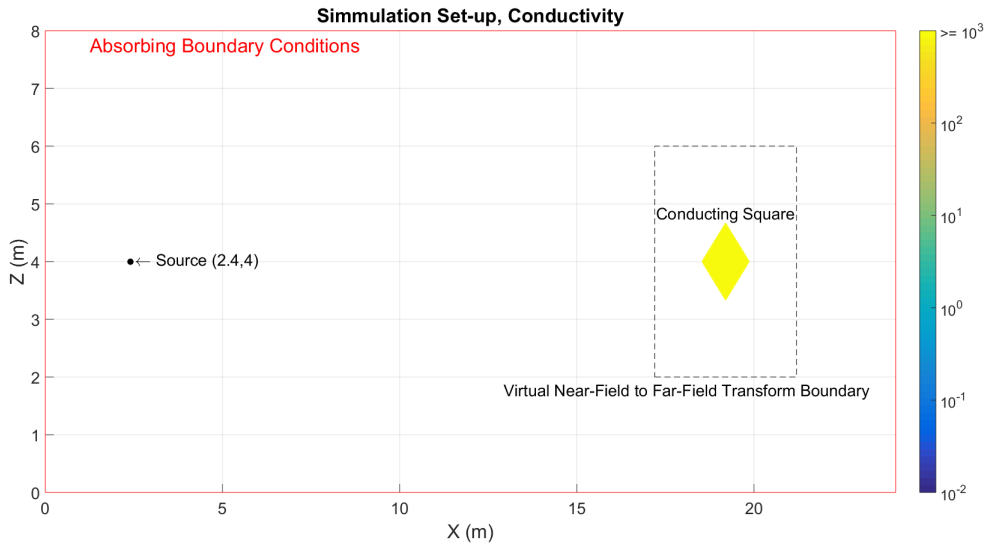

Figure 10. The computational set-up for the 600 MHz conducting square RCS verification run

The 600 MHz frequency was chosen as the higher frequency creates a more feature rich bistatic radar cross section that allows for a more robust feature comparison than that of the lower frequencies. The bistatic RCS obtained from this calculation is shown in Figure 11. The magnitude of the radar cross section was not corrected for distance from the source, the reference paper did not specify how they normalized their calculated bistatic cross sections so only a comparison between shapes of the

curves is valid, not absolute values. Visual inspection of the 300 MHz and 600 MHz cases from page 5798 in the reference paper [14] shows that our obtained bistatic RCS appears to fall somewhere between those two cases. Remember that the point source used in this study, although far away still does not perfectly represent the plane wave used in the reference paper so some difference is to be expected. Due to the similarity of the general pattern and symmetry with the reference cases the code was considered physically valid until the use of a plane wave source in the code can be properly implemented for full verification.

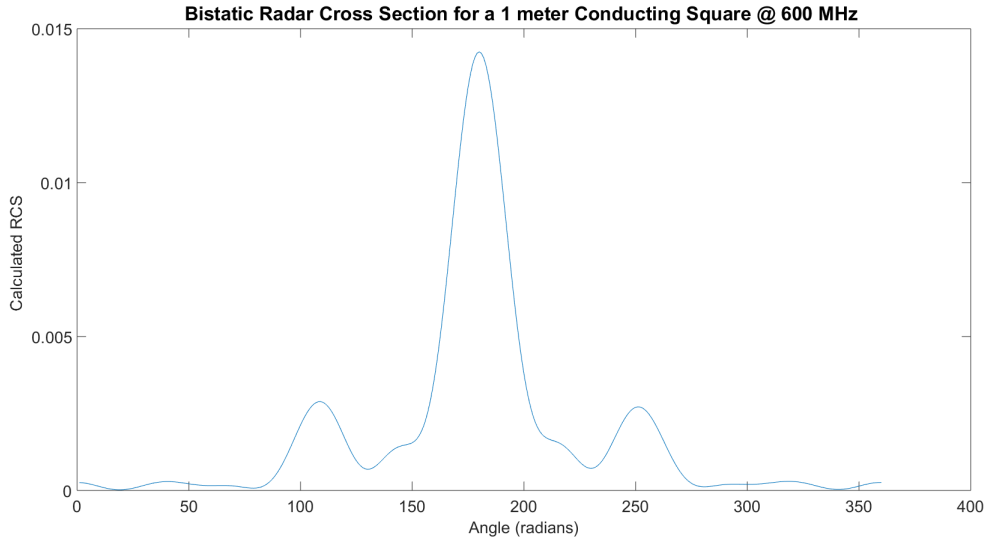

Figure 11. The bistatic radar cross section obtained from the code for a frequency of 600 MHz

IV. Analysis

4.1 LAURA Results

The resulting data from the LAURA simulation was imported into MATLAB and post-processed to calculate plasma and electron-neutral and electron-ion collision frequencies for each simulation point on the grid. The total electron-neutral and electron-ion collision frequencies were calculated based on sum of the semi-empirical relations for each species given in [16] and [17, pg. 104]. The resulting index of refraction and skin depth plots in Figures 12 through 19 are four of the thirteen total converged simulations run for this study. Index of refraction was calculated using Equation 44. Skin depth is calculated from the inverse of the imaginary component of k and represents the distance for a electromagnetic wave to attenuate 36.8% in a material, a higher skin depth means less attenuation, a vacuum has an infinite skin depth.

$$\nu_{ei} = \frac{54.5 n_i Z_i^2}{T_e^{3/2}} \tag{161}$$

Table 5. Semi-empirical relations for the electron neutral collision frequency

Species	ν_{en} (Hz)
N_2	$2.33 \times 10^{-11} n(N_2)(1 - 1.21 \times 10^{-4} T_e) T_e$
O_2	$1.82 \times 10^{-10} n(O_2)(1 + 3.6 \times 10^{-2} T_e^{1/2}) T_e^{1/2}$
O	$2.8 \times 10^{-10} n(O) T_e^{1/2}$

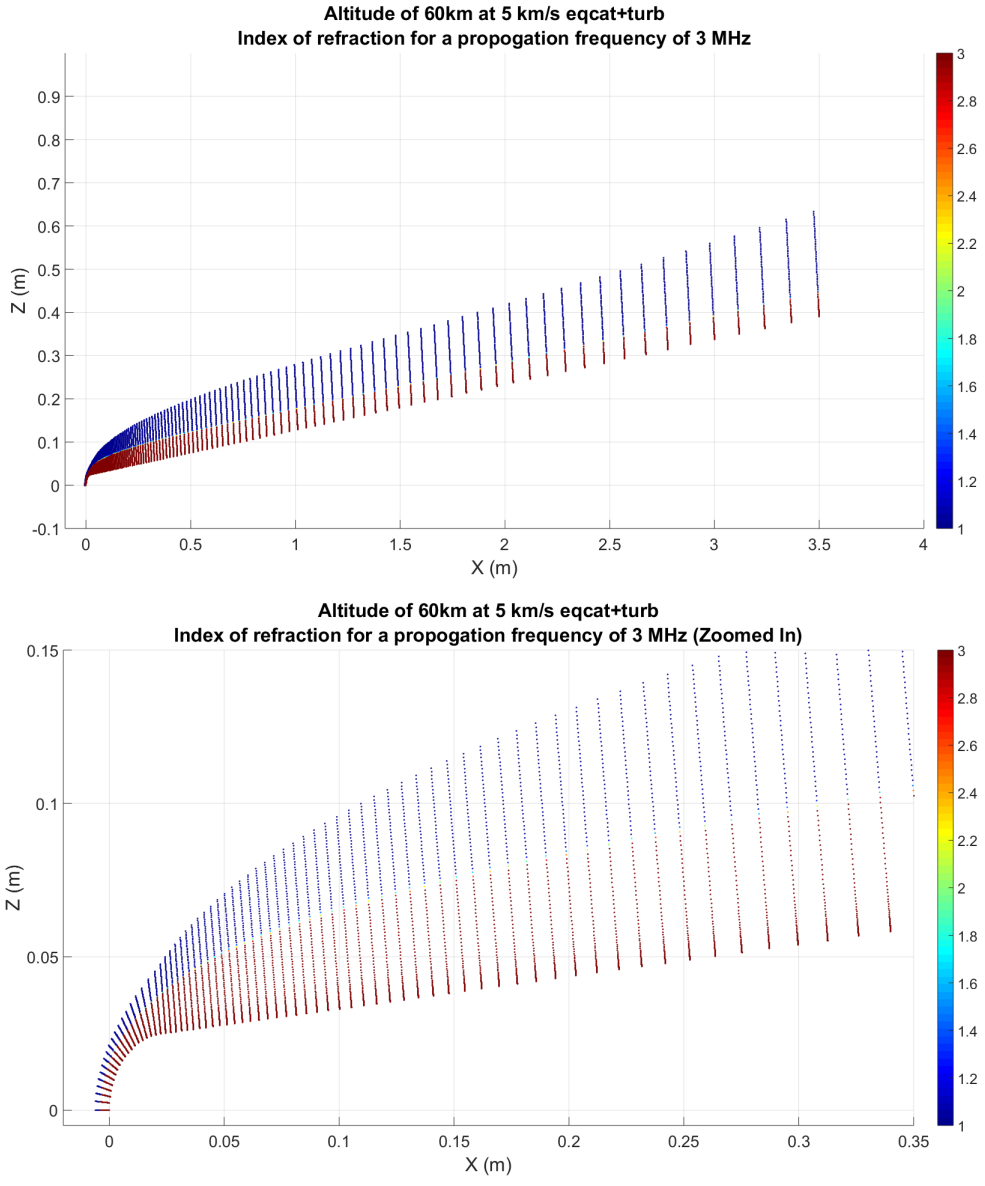

Figure 12. Example of the index of refraction of plasma calculated from LAURA simulations at 60 km 5 km/s

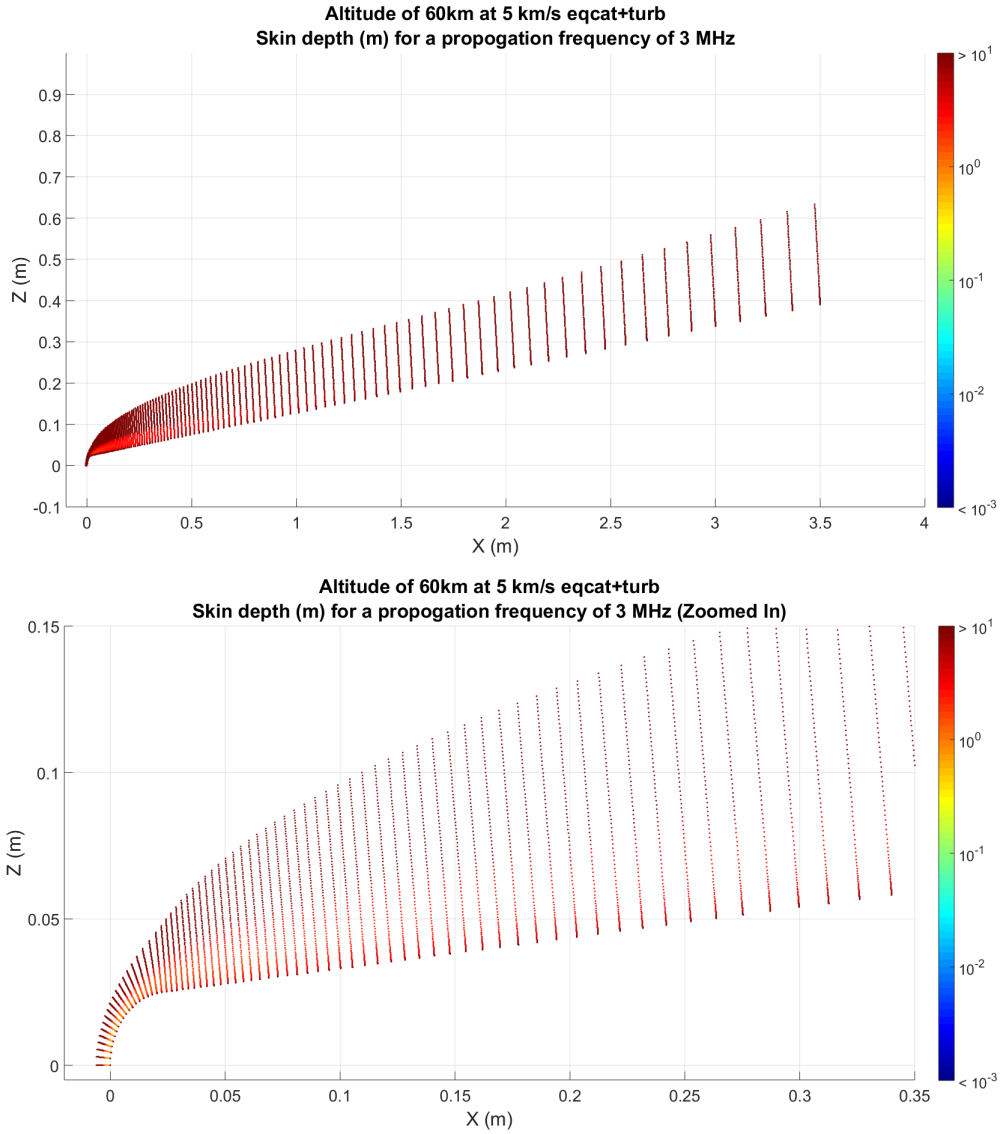

Figure 13. Example of the skin depth of plasma calculated from LAURA simulations at 60 km 5 km/s

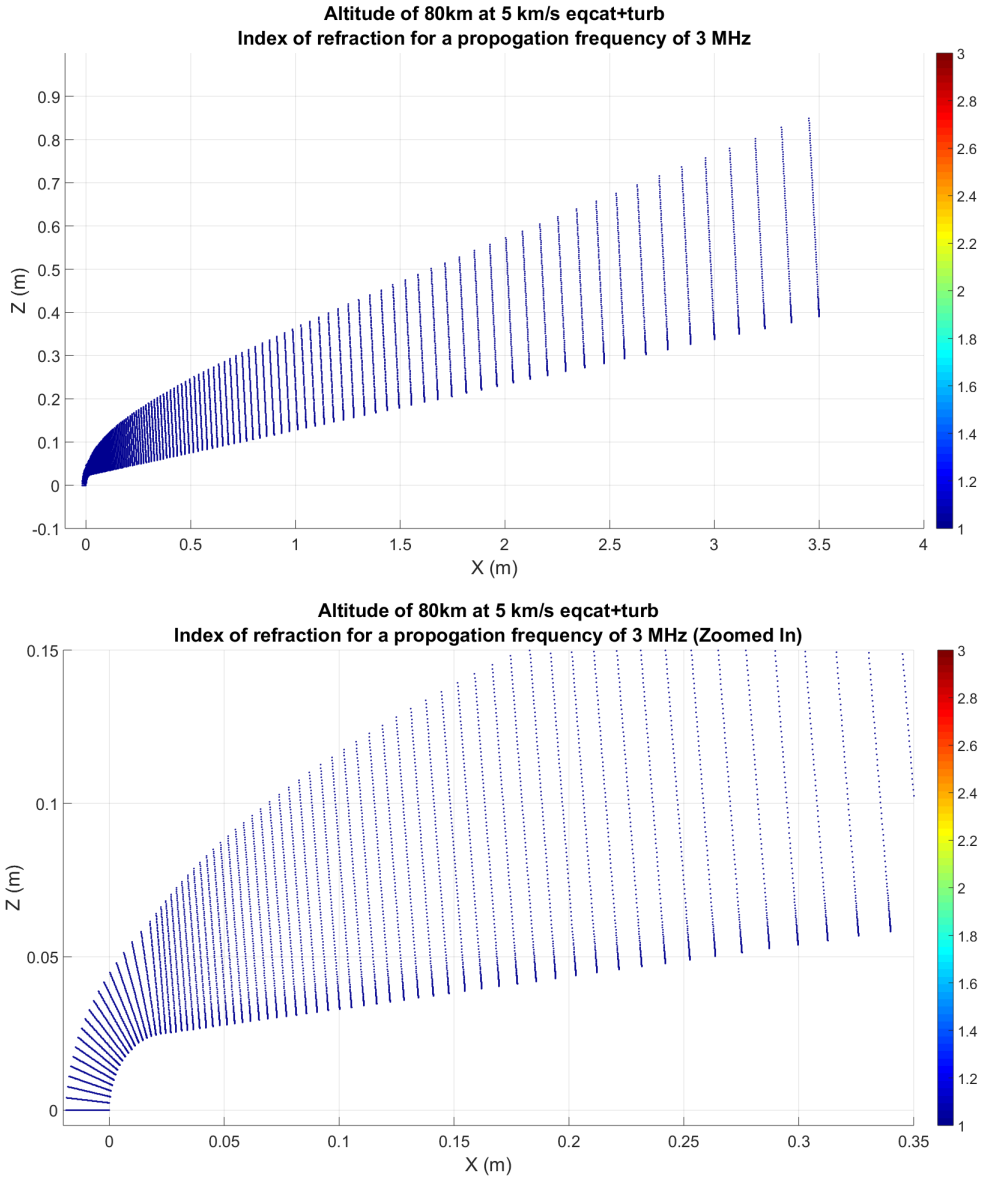

Figure 14. Example of the index of refraction of plasma calculated from LAURA simulations at 80 km 5km/s

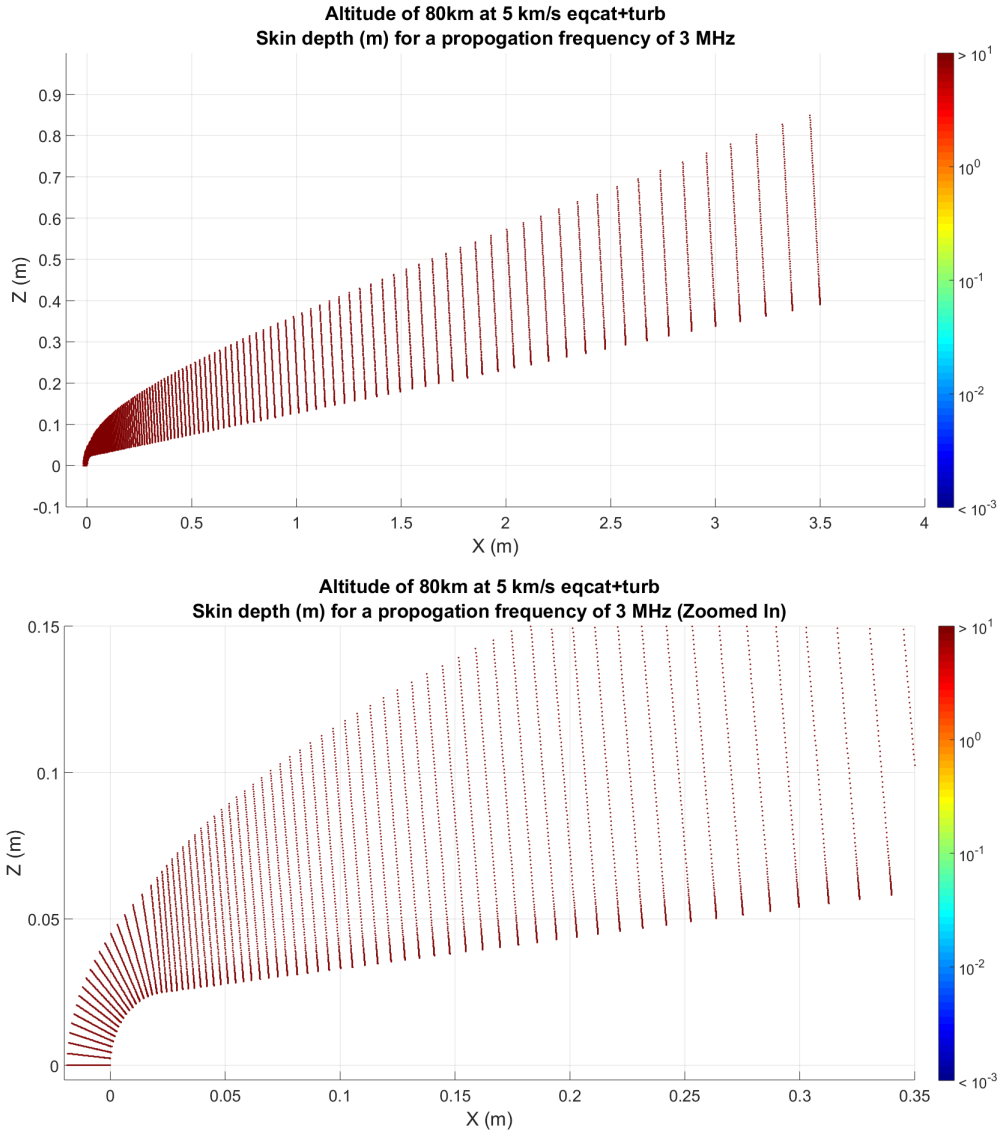

Figure 15. Example of the skin depth of plasma calculated from LAURA simulations at 80 km 5km/s

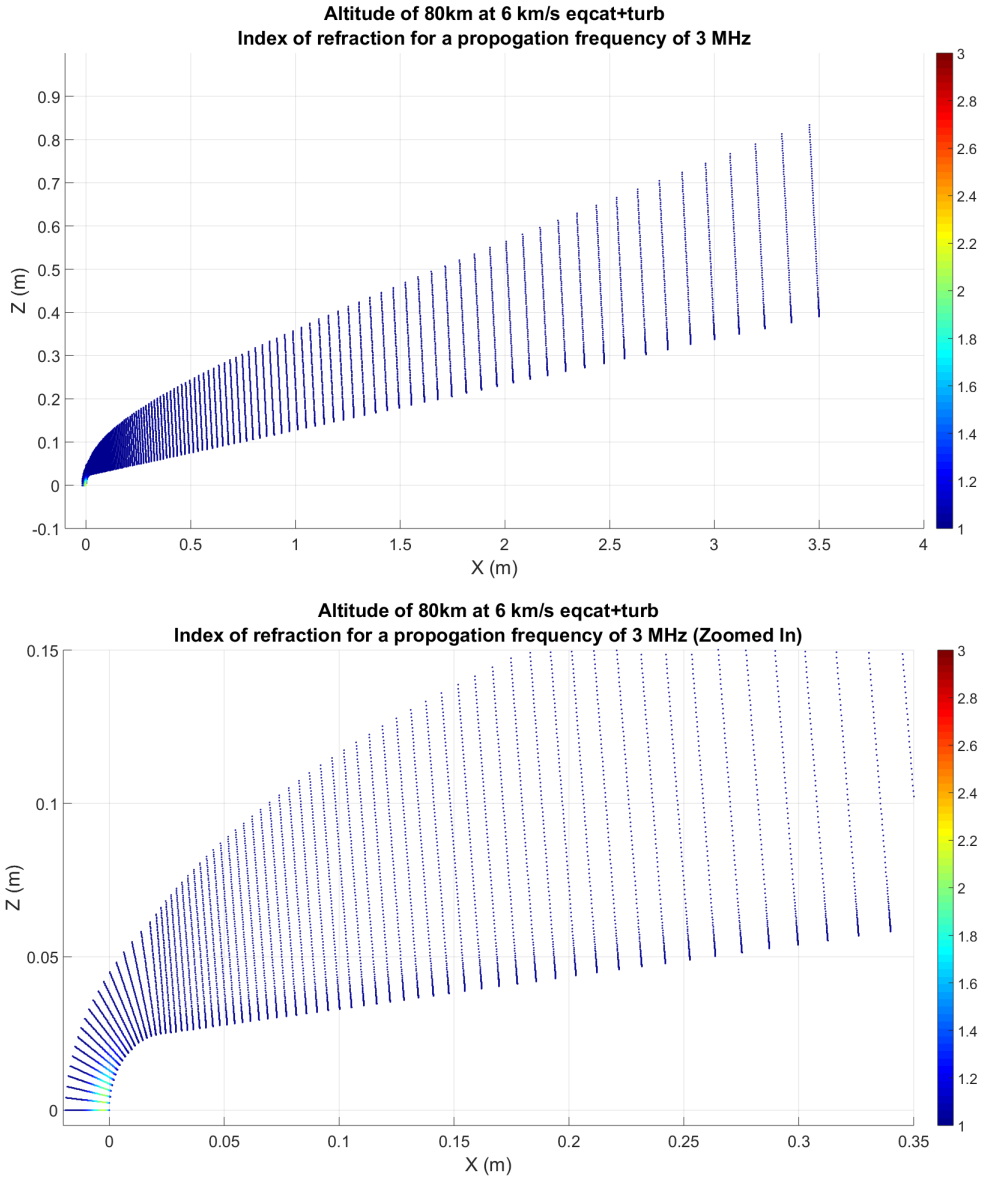

Figure 16. Example of the index of refraction of plasma calculated from LAURA simulations at 80 km 6 km/s

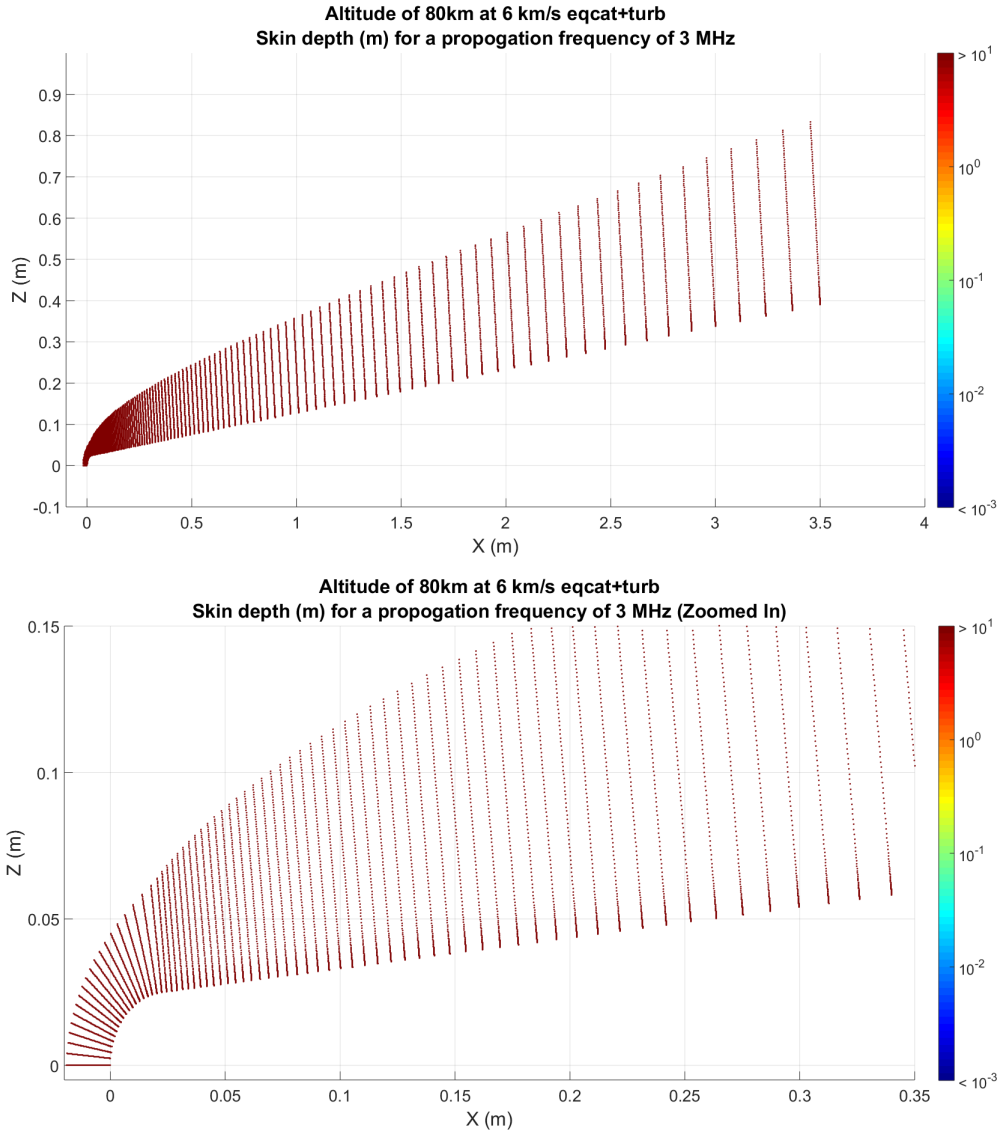

Figure 17. Example of the skin depth of plasma calculated from LAURA simulations at 80 km 6 km/s

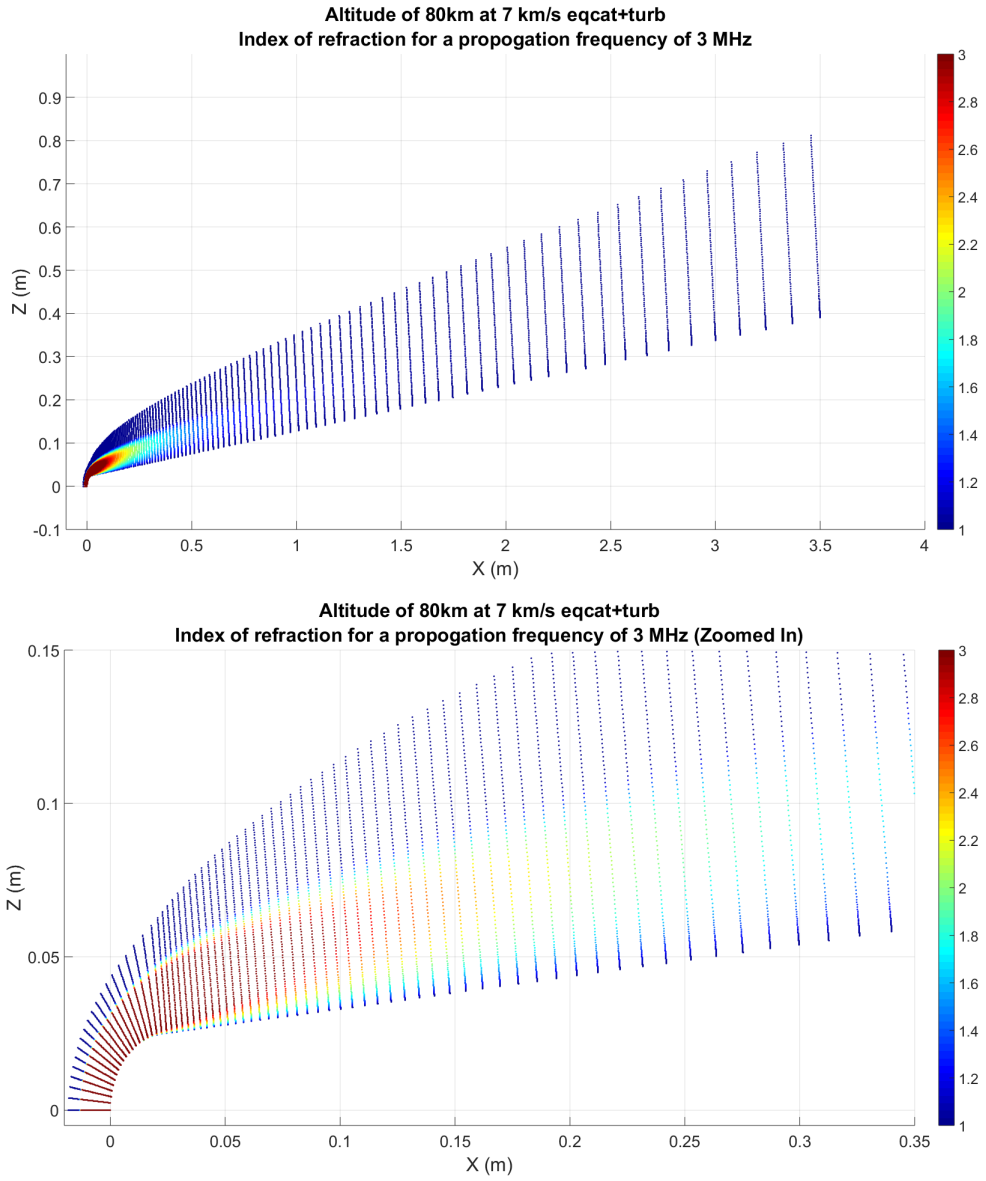

Figure 18. Example of the index of refraction of plasma calculated from LAURA simulations at 80km 7 km/s

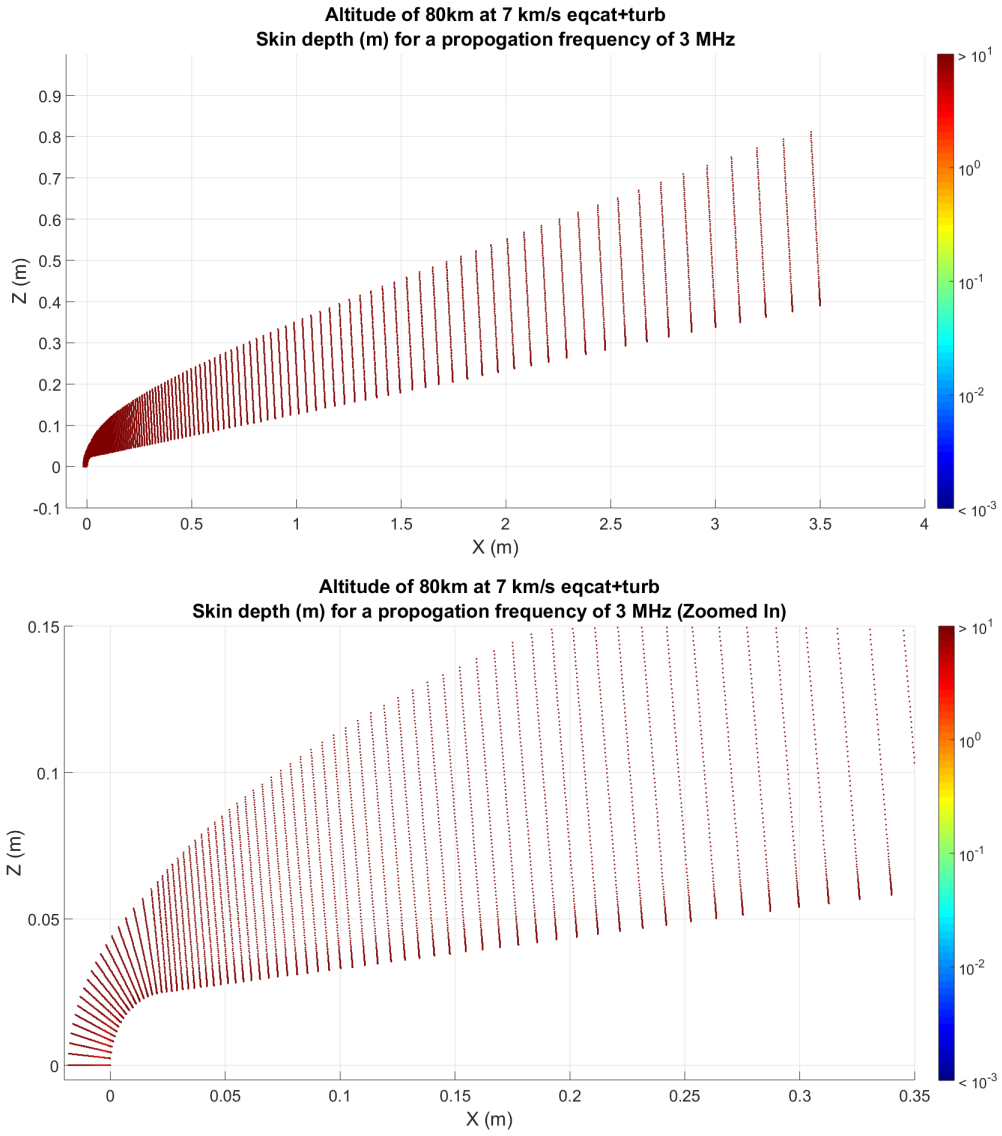

Figure 19. Example of the skin depth of plasma calculated from LAURA simulations at 80km 7 km/s

These four LAURA simulations represent the simulation conditions which obtained satisfactory convergence with the additional simulation parameters of a shear-stress transport turbulence model and an equilibrium catalytic surface boundary conditions not accounted for in the original nine simulations. The plots consist of a plot of the calculated skin depth around the blunted cone and the calculated index of refraction both for the entire vehicle and then just the front 10%. A relatively lower

skin depth attenuates the wave more which means a lower radar cross section as the plasma acts to absorb energy from the wave. The calculated index of refraction determines at what point the incident radar wave will reflect, in all cases there is negligible skin depth attenuation effects indicating we should expect minimal energy absorption by the plasma. The simulations lower in altitude and the higher speed seem to be correlated with a higher index of refraction in the plasma indicating we would expect the hypersonic vehicle to have a larger effective radar cross section than it would without the plasma sheath as it increases the effective reflecting body.

4.2 RCS Results

A total of thirteen FDTD simulations were run to calculate the relative RCS using the plasma conditions obtained from the LAURA simulation. The simulations were run on a 3.30 GHz Intel Xeon E3-1226 CPU with 8 GB of installed RAM using MATLAB R2015a. A grid size of 300 $\times$ 300 points was used to represent an 8 m $\times$ 8 m area, giving a dx and dz of 0.02667 m each and a dt of 3.1422e-11 seconds. The run time for each simulation was 4.45 hours to reach a convergence limit of less than 0.1% change in the total energy field in the simulation space. The simulation calculates the relative RCS by first running the simulation with free space surrounding the blunted cone, and subsequently with the calculated plasma sheath surrounding the blunted cone, the bistatic cross section for the plasma sheathed cone is divided by the cross section obtained for the cone in free space to obtain the relative change in the RCS caused by the plasma sheath. As mentioned previously, frequency scaling was used to enlarge the plasma sheath area in the simulation and increase detail. These RCS calculations are valid for the specified cone dimensions and a propagation frequency of 30 MHz. The bistatic angle is measured counter-clockwise from a vector created by drawing a line from the source to the tip of the cone. Additionally since only the

tip of the hypersonic cone was simulated only the RCS values between 100 and 260 degrees are considered representative. Angles outside of this range would likely be heavily influenced by the unsimulated wake region. The plots of the bistatic cross section for three interesting cases are shown in Figures 20 through 22 the remaining cases studied are in the appendix:

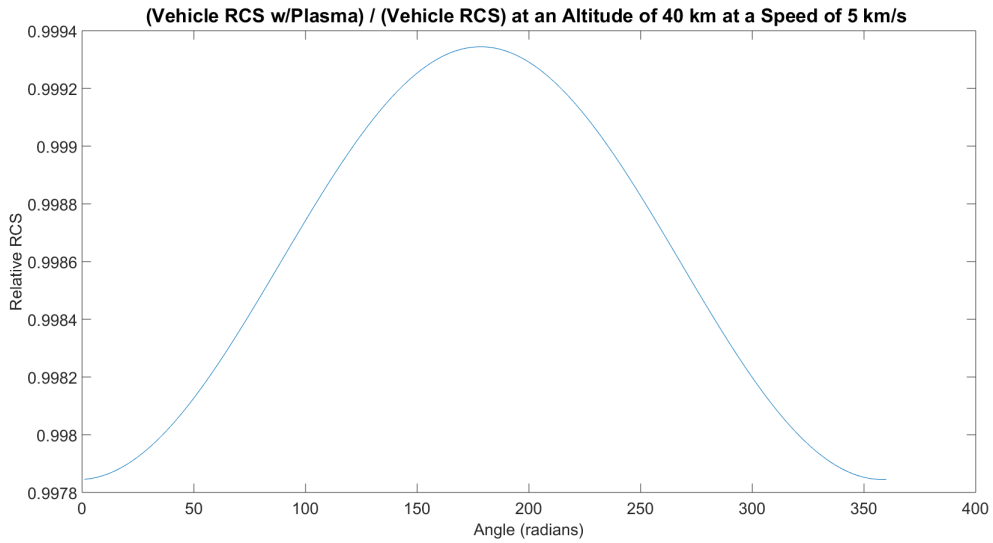

Figure 20. Relative radar cross section results at 30 MHz for an altitude of 40km and a speed of 5 km/s

Note due to the lack of inclusion of wake region effects in this study RCS values below 100 and above 260 degrees are not considered realistic.

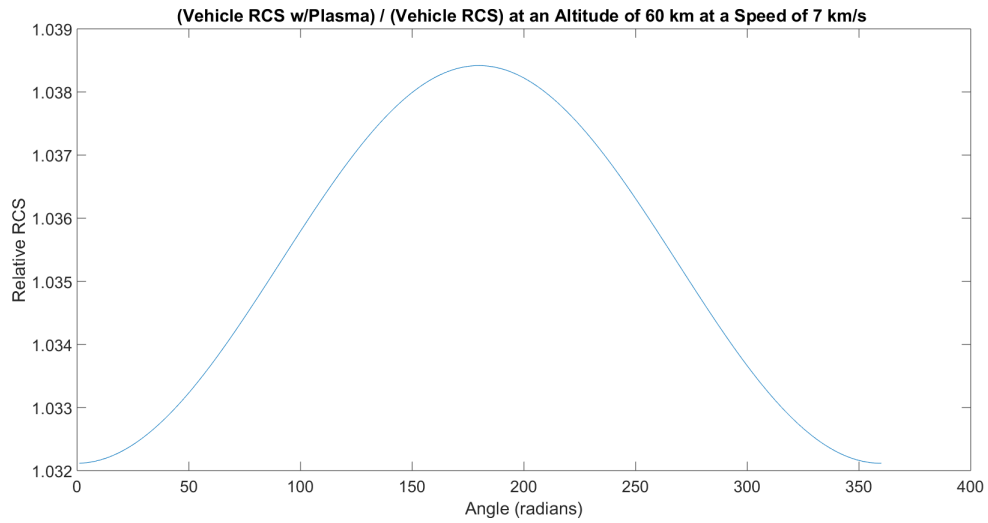

Figure 21. Relative radar cross section results at 30 MHz for an altitude of 60km and a speed of 7 km/s

Note due to the lack of inclusion of wake region effects in this study RCS values below 100 and above 260 degrees are not considered realistic.

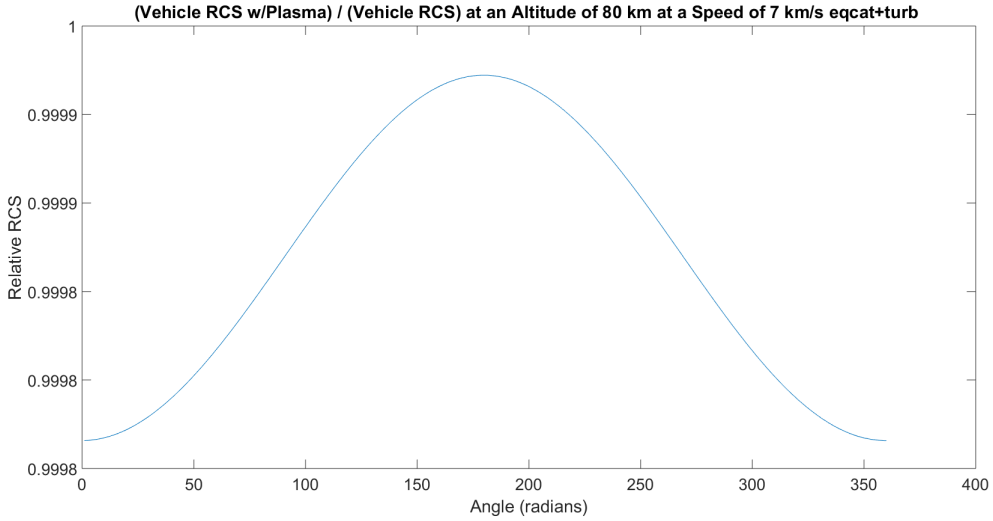

Figure 22. Relative radar cross section results at 30 MHz for an altitude of 80km and a speed of 7 km/s

This simulation includes equilibrium catalytic boundary condition at the body surface and the mentor SST turbulence model. Note due to the lack of inclusion of wake region effects in this study RCS values below 100 and above 260 degrees are not considered realistic.

These three cases were highlighted for discussion because the 40 km at 5 km/s and 80 km at 7 km/s cases are those which showed possible 'reduction' in RCS at their specific altitudes, and the 60 km case had the largest increase in RCS out of all 9 cases. The main conclusion drawn from these results is that in general the larger the electron density around the hypersonic cone the larger its conductive area which means the wave reflects off of a larger conductive object corresponding a larger RCS. These results show that although there have been a number of studies on the potential energy absorption effects of a hypothetical plasma sheath, the dominant mechanism of interaction under the hypersonic conditions simulated in this study is RCS increase rather than decrease due to the sharp increase of electron density at the shock front of the hypersonic cone and the lower frequencies of OTHR [18] [19] [20] [21].

One possible physical explanation for the reduced RCS in the 40 km altitude at 5 km/s case is that although there is some electron density build up around the blunted cone, being at a lower altitude the particle density is much higher than at the higher altitude cases so the larger collision frequency acts to dampen the electric field slightly as it is reflected. At higher speeds for the 40 km altitude the electrons density increases sharply enough so that the wave is reflected before it can noticeably attenuate and the conductive enlarging effect leads to a relative increase in RCS. For the 80 km at 7 km/s case, there is just enough electron density to slightly interact and dampen the wave via the collision process, the lower speeds at 80 km altitude have low enough electron density that there is essentially no interaction with the wave and the RCS appears the same as that of the bare hypersonic cone. These trends would agree with those previously shown Figure 3. However since these reductions were of such small orders of magnitude further studies with a more refined grid could help determine whether these effects were truly physical or due to some sort of numerical error.

V. Conclusion

Using a two step process of first determining the plasma conditions of a hypersonic plasma sheath, and subsequently propagating an incident electromagnetic wave at the sheathed vehicle the effect of the sheath on the vehicle's RCS was computationally calculated. The simulated electromagnetic scattering off of the tip of a plasma sheathed hypersonic cone in general was found to yield an relative RCS due to the increased area of conductivity around the object provided by its plasma sheath. This indicates under the simulated conditions the plasma was acting primarily reflective rather than attenuative in nature. Two noted exceptions were found where a potential decrease in relative RCS was calculated, however these decreases were small in nature and may require more detailed study to be conclusive. The maximum increase occurred at 60 km in altitude at 7 km/s at 3.84% and the relative decreases were found at 40 km altitude with a speed of 5 km/s and at 80 km altitude with a speed of 7 km/s, with the relative decrease at 40 km being the larger of the two at 0.1%.

There are a number of additional topics of interest in this problem that were not included in this study should be the subject of future work. Principle among possible expansions of this study is the incorporation of the extended plasma wake region following the tail of the hypersonic body. If this wake region has a large enough electron density to interact with the incident electromagnetic field its longer length could lead to complex and interesting resonance region scattering. Another valuable extension of this study would be the inclusion of multiple angles of attack which could drastically change the electron density distribution around the vehicle. More complex considerations could also include: the possible dynamic fluctuation in the plasma characteristics in time, the seasonal and other variances in the upper atmosphere, higher order plasma dampening and collisional models, and the effects of various ablation materials.

This study takes the first step at developing a comprehensive flexible framework to integrate data from a simulated hypersonic plasma sheath to determine how it interacts with incident and potentially outgoing electromagnetic radiation. Hypersonic vehicle testing has become more prominent in practice and theory as technology advances. A tool to help characterize the potential electromagnetic effects they may encounter should provide insights for designing and planning experimental tests.

VI. Appendix

6.1 Example LAURA Namelist File

```
&laura_namelist
velocity_ref = 5000.0 ! reference velocity, m/s
density_ref  = 0.000288 ! reference density, kg/m^3
tref         = 245 ! reference temperature, K
alpha        = 0.0 ! pitch angle, degrees
twall_bc     = 500.0 ! initial wall temperature, K
chem_flag  = 1 ! 0 chemically frozen, 1 chemical source on
therm_flag = 1 ! 0 thermally frozen,  1 thermal source on
irest   = 1 ! 0 for fresh start, 1 for restart
ncyc  = 20000 ! global steps
jupdate = 4 ! steps between update of jacobian
ntran   = 4 ! steps between update of transport properties
nitfo =  0 ! number of 1st-order relaxation steps
iterwrt = 400 ! steps between saves of intermediate solution
rf_inv = 2.0 ! inviscid relaxation parameter
rf_vis = 1.0 ! viscous relaxation parameter
movegrd = 0 ! number of steps between calls to align_shock
maxmoves =  0 ! maximum number of calls to align_shock
re_cell = 0.1 ! target cell reynolds number at wall
fsh = 0.6 ! target bow shock position arc length fraction
kmax_error  = 0.01 ! error norm triggering k-cell increase
kmax_final  = 128   ! final number of k-cells
nexch    = 2 ! steps between exchange of info in mpi
frac_line_implicit = 0.7 ! fraction of line by block tri-dia
surface_temperature_type_0 = 'radiative equilibrium'
catalysis_model_0 = 'equilibrium-catalytic'
turb_model_type = 6
emiss_a_0 = 0.89
ept = 0.010 ! relaxation factor on read eq wall bc
point_implicit  = .true.
dimensionality = 'axisymmetric'
xmc =    2.3333
ymc =    0.0000
zmc =    0.0000
grid_conversion_factor =    1.0000
sref =   0.66494E-02
cref =    3.5000
/
```

Figure 23. Example of a LAURA namelist file for the 60 km altitude 5 km/s case including turbulence

6.2 Explanation of LAURA Namelist File

Table 6. Explanation of LAURA Namelist Parameters

Flag	Default Value	Meaning	Units
velocity_ref	XXXXX	This is the velocity of the far-field flow stream for the simulation	m/s
density_ref	XXXXX	This is the density of the far-field flow stream for the simulation	kg/m^3
tref	200	This is the temperature of the far-field flow stream for the simulation	K
alpha	0	This is the angle of attack which indicates the angular difference between the reference axis indicating the objects orientation and the free stream velocity vector	degrees
twall_bc	500	This is the initial temperature of the solid surface boundary condition	K
chem_flag	1	Turn on or off chemical source calculating for nonequilibrium flow	-
therm_flag	1	Turn on or off thermal source calculating for nonequilibrium flow	-

irest	0	Determines whether to continue solution calculations from laura.rst (irest=0) or to restart using free stream values (irest=1)	-
ncyc	1000	Number of full cycle iterations	-
jupdate	10	Number of cycles between updating the jacobian, which is the matrix relationship of various variables with each other	-
ntran	1	Number of cycles before refreshing the transport equations based on newly calculated properties	-
nitfo	0	Number of steps run with only 1st order approximations. Useful for faster simulation initialization before high order approximations are used for more detailed convergence	-
iterwrt	200	Number of steps run between saving of partial output files	-
rf_inv	3	Inviscid relaxation factor, a weighting that helps to 'average' the newly calculated values in the iterative process with the prior iteration to help convergence.	-

rf_vis	1	Viscous relaxation factor, a weighting that helps to 'average' the newly calculated values in the iterative process with the prior iteration to help convergence.	-
movegrd	0	Number of cycles between calculating various grid alignment parameters, 0 means no grid alignment calculations are done. Grid alignment seeks to modify the location of the free stream boundary based on bow shock location via align_shock	-
maxmoves	0	Maximum number of grid adaptation calls in a run.	-
re_cell	0.1	Determines the goal cell Reynolds number at a wall after a grid movement. In essence it defines the proper scaling of cell scaling at a wall based on flow properties.	-
fsh	0.8	Determines the relative distance between surface and inflow where the bow shock is expected	-

kmax_error	0.01	Increases cells in k direction by an amount kmax_factor when the global L2 error norm reaches this value until the maximum number kmax_final is reached.	-
kmax_final	0	Goal number of cells in the k direction.	-
nexch	2	Number of cycles between combining parallel process to update cell conditions	-
frac_line_implicit	0.7	Designates the fraction of line-implicit to be used in relaxation	-
surface_temperature_type_0	'constant'	Designates which model to use for surface temperature	-

6.3 Relative RCS Results

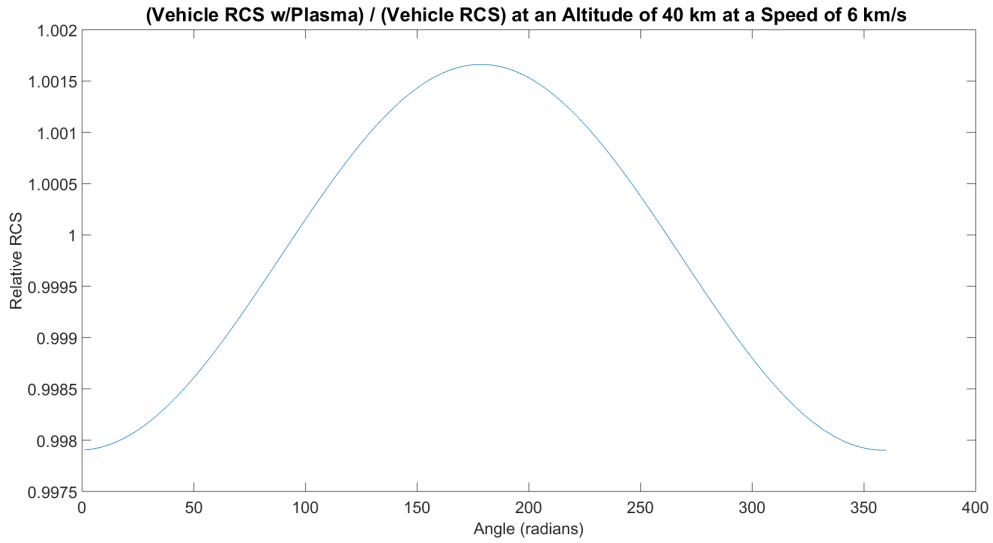

Figure 24. Relative radar cross section results at 30 MHz for an altitude of 40km and a speed of 6 km/s

Note due to the lack of inclusion of wake region effects in this study RCS values below 100 and above 260 degrees are not considered realistic.

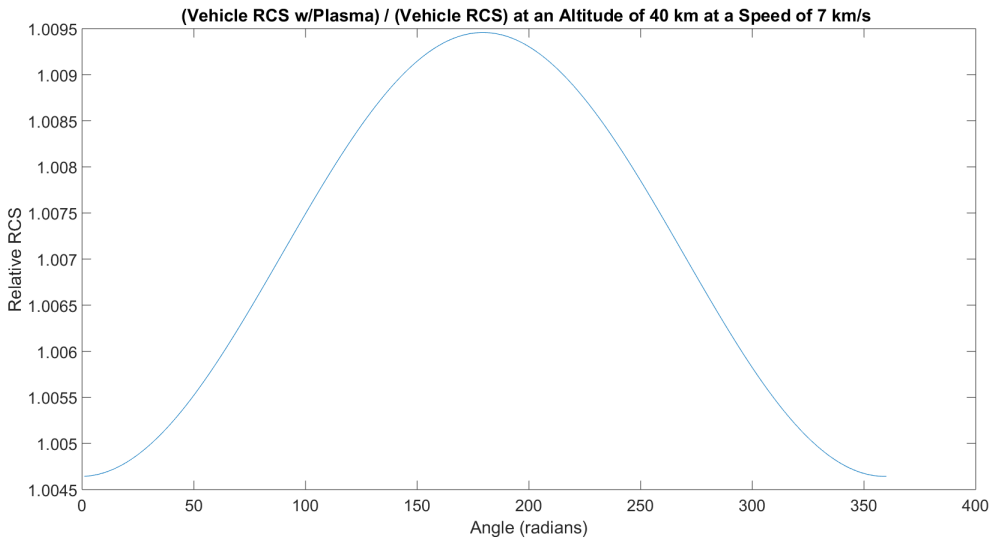

Figure 25. Relative radar cross section results at 30 MHz for an altitude of 40km and a speed of 7 km/s

Note due to the lack of inclusion of wake region effects in this study RCS values below 100 and above 260 degrees are not considered realistic.

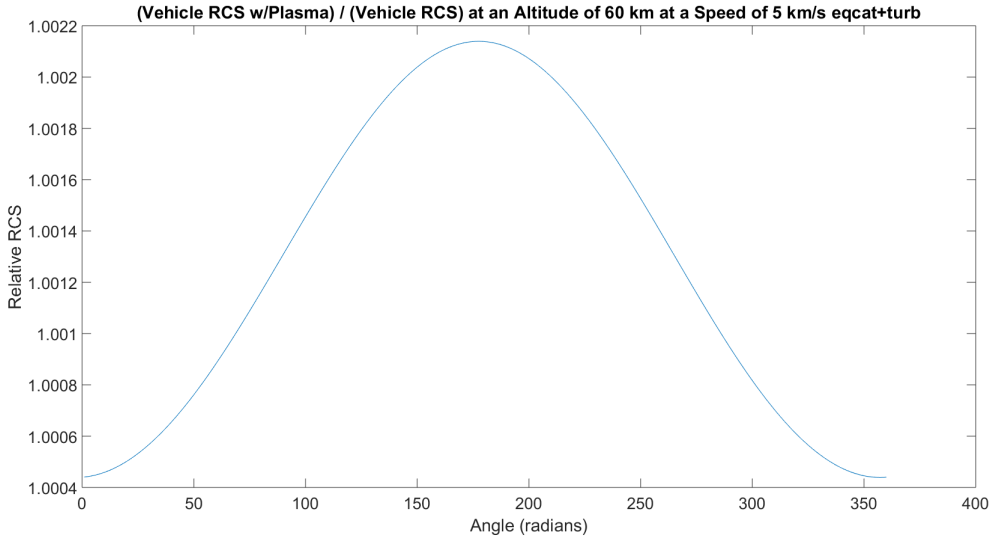

Figure 26. Relative radar cross section results at 30 MHz for an altitude of 60km and a speed of 5 km/s

This simulation includes equilibrium catalytic boundary condition at the body surface and the mentor SST turbulence model. Note due to the lack of inclusion of wake region effects in this study RCS values below 100 and above 260 degrees are not considered realistic.

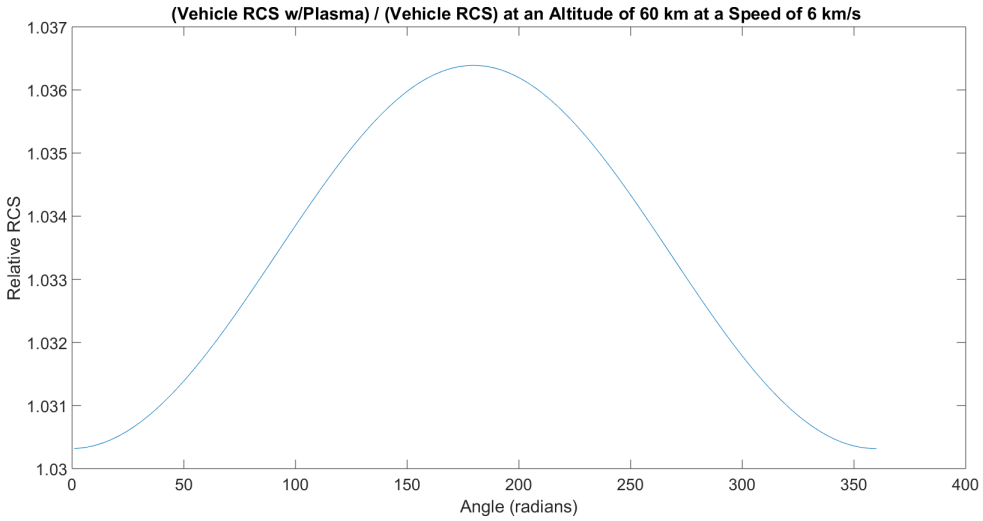

Figure 27. Relative radar cross section results at 30 MHz for an altitude of 60km and a speed of 6 km/s

Note due to the lack of inclusion of wake region effects in this study RCS values below 100 and above 260 degrees are not considered realistic.

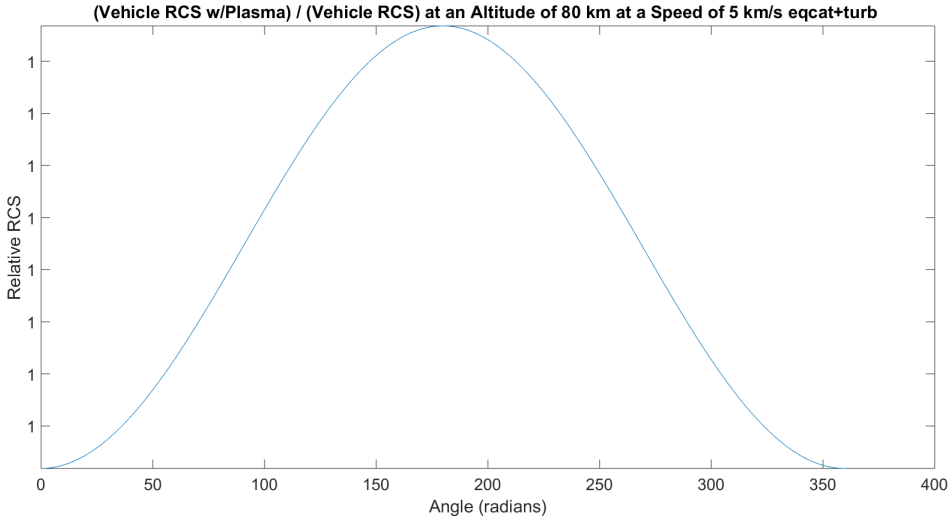

Figure 28. Relative radar cross section results at 30 MHz for an altitude of 80km and a speed of 5 km/s

This simulation includes equilibrium catalytic boundary condition at the body surface and the mentor SST turbulence model. Note due to the lack of inclusion of wake region effects in this study RCS values below 100 and above 260 degrees are not considered realistic.

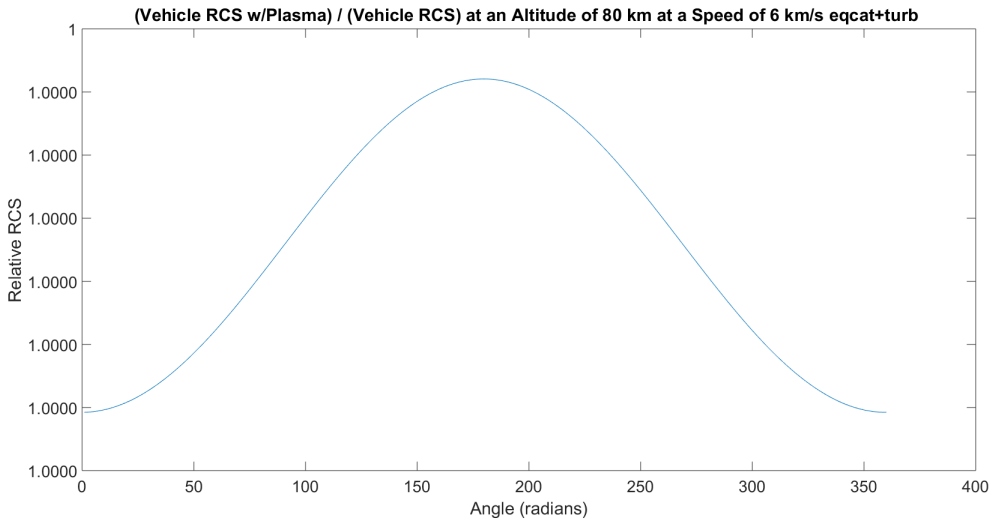

Figure 29. Relative radar cross section results at 30 MHz for an altitude of 80km and a speed of 6 km/s

This simulation includes equilibrium catalytic boundary condition at the body surface and the mentor SST turbulence model. Note due to the lack of inclusion of wake region effects in this study RCS values below 100 and above 260 degrees are not considered realistic.

Bibliography

1. L. Saalman, "Factoring russia into the us-chinese equation on hypersonic glide vehicle," *SIPRI*, 2017.

2. National Academy of Sciences, Engineering, and Medicine, "A threat to america's global vigilance, reach, and power - high-speed, maneuvering weapons: Unclassified summary," *The National Academies Press*, 2016.

3. 114th Congress, "National defense authorization act for fiscal year 2017, h. r. 4909," 2016.

4. B.-Y. Liu, "Hf over-the-horizon radar system preformance analysis," mathesis, Naval Postgraduate School, Sep. 2007.

5. J. T. G.-H. Y. C. Liu, *Computational Fluid Dynamics A Practical Approach*, 2nd ed. Butterworth-Heinemann, 2013.

6. D. C. Wilcox, "Formulation of the k-ω turbulence model revisited," *AIAA Journal*, 2008.

7. E. F. Knott, J. F. Shaeffer, and M. T. Tuley, *Radar Cross Section.* Scitech Publishing, Inc., 2004.

8. A. E. V. Demir, *The Finite-Difference Time-Domain Method for Electromangetics with MATLAB Simulations.* SciTech Publishing, 2009.

9. A. T. S. C. Hagness, *Computational Electrodynamics The Finite-Difference Time-Domain Method.* ARTECH HOUSE, 2005.

10. B. E. A. Majda, "Absorbing boundary conditions for the numerical simulation of waves," *Mathematics of Computation*, vol. 31, no. 139, pp. 629–651, 1977.

11. G. Mur, "Absorbing boundary conditions for the finite-difference time-domain electromagnetic-field equations," *IEEE Transactions on Electromangetic Compatibility*, vol. EMC-23, no. 4, 1981.

12. P. A. Gnoffo, "Upwind-biased, point-implicit relaxation strategies for viscous, hypersonic flows," *9th Computational Fluid Dynamics Confrence*, 1989.

13. A. M. P. A. G. C. O. J. W. L. Kleb, *LAURA Users Manual: 5.5-64987*, NASA Langley Research Center, Feb. 2013. [Online]. Available: https://ntrs.nasa.gov/archive/nasa/casi.ntrs.nasa.gov/20130009520.pdf

14. F. E. Yardim and N. Akcam, "Estimation of the radar cross-section in rayleigh, mie, and optical regions by the 2-d-fdtd simulation," *IEEE Transactions on Antennas and Propagation*, 2014.

15. M. A. Ordal, L. L. Long, R. J. Bell, S. E. Bell, R. R. Bell, J. R. W. Alexander, and C. A. Ward, "Optical properties of the metals al, co, cu, au, fe, pb, ni, pd, pt, ag, ti, and w in the infrared and far infrared," *Applied Optics*, 1983.

16. P. Banks, "Collision frequencies and energy transfer electrons," *Planetary and Space Science*, vol. 14, pp. 1085–1103, 1966.

17. R. S. A. Nagy, *Ionospheres*, 2nd ed. Cambridge University Press, 2009.

18. B. Bai, X. Li, J. Xu, and Y. Liu, "Reflections of electromagnetic waves obliquely incident on a multilayer stealth structure with plasma and radar absorbing material," *IEEE Transactions on Plasma Science*, 2015.

19. C. Shao, L. Nie, and W. Chen, "Analysis of electromagnetic scattering characteristics for a htv-2 type flight vehicle ablation flows," *AIP Confrence Proceedings*, 2014.

20. A. Rokhlenko, "The reflection of electromagnetic waves by a conducting surface shielded with a plasma layer," *IEEE Transactions on Plasma Science*, 2002.

21. R. J. Vidmar, "On the use of atmospheric pressure plasmas as electromagnetic reflectors and absorbers," *IEEE Transactions on Plasma Science*, 1990.

REPORT DOCUMENTATION PAGE

Form Approved
OMB No. 0704–0188

1. REPORT DATE *(DD–MM–YYYY)*	2. REPORT TYPE	3. DATES COVERED *(From — To)*
23–03–2017	Master's Thesis	Jun 2015 — Mar 2017

4. TITLE AND SUBTITLE

A Computational Study: The Effect of Hypersonic Plasma Sheaths on Radar Cross Section for Over the Horizon Radar

5a. CONTRACT NUMBER

5b. GRANT NUMBER

5c. PROGRAM ELEMENT NUMBER

6. AUTHOR(S)

Zachary W. Hoeffner, 1st Lieutenant, USAF

5d. PROJECT NUMBER

5e. TASK NUMBER

5f. WORK UNIT NUMBER

7. PERFORMING ORGANIZATION NAME(S) AND ADDRESS(ES)

Air Force Institute of Technology
Graduate School of Engineering and Management (AFIT/EN)
2950 Hobson Way
WPAFB OH 45433-7765

8. PERFORMING ORGANIZATION REPORT NUMBER

AFIT-ENP-MS-17-M097

9. SPONSORING / MONITORING AGENCY NAME(S) AND ADDRESS(ES)

National Air and Space Intelligence Center
4180 Watson Way
WPAFB OH 45433
DSN 787-7809, COMM (937) 257-7809

10. SPONSOR/MONITOR'S ACRONYM(S)

NASIC

11. SPONSOR/MONITOR'S REPORT NUMBER(S)

12. DISTRIBUTION / AVAILABILITY STATEMENT

DISTRIBUTION STATEMENT A.
APPROVED FOR PUBLIC RELEASE; DISTRIBUTION UNLIMITED.

13. SUPPLEMENTARY NOTES

14. ABSTRACT

In this study radar cross sections were calculated for an axial symmetric 6-degree half angle blunted cone with a nose radius of 2.5 cm and length of 3.5 m including and excluding the effects of an atmospheric hypersonic plasma sheath for altitudes of 40 km, 60 km and 80 km and speeds of 5 km/s, 6 km/s and 7 km/s. LAURA, was used to determine the plasma characteristics for the hypersonic flight conditions using a 11-species 2-temperature chemical model. Runs were accomplished first with a super-catalytic surface boundary condition without a turbulence model and then for some cases with an non-reactive surface boundary condition where a mentor-SST turbulence model was used. The resulting plasma sheath properties were used in a Finite Difference Time Domain code to calculate the cones radar cross section both with and without the effects of the plasma sheath. The largest increase in radar cross section (RCS) was found for the 60 km 7km/s case with an increase of 3.84%. A possible small decrease in RCS was found for the 40 km altitude 5 km/s and 80 km 7 km/s cases on the order of 0.1%

15. SUBJECT TERMS

Hypersonic, Plasma, Radar

16. SECURITY CLASSIFICATION OF:			17. LIMITATION OF ABSTRACT	18. NUMBER OF PAGES	19a. NAME OF RESPONSIBLE PERSON
a. REPORT	b. ABSTRACT	c. THIS PAGE			Maj Charlton D. Lewis, AFIT/ENP
U	U	U	SAR	99	19b. TELEPHONE NUMBER *(include area code)* (937) 255-3636, x4555; charlton.lewis@afit.edu